VolFe: an open-source tool for calculating melt-vapor equilibria including silicate melt, carbon, hydrogen, sulfur, and noble gases

Ery C. Hughes: Te Pū Ao GNS Science (e.hughes@gns.cri.nz)
Philippa Liggins: University of Oxford
Penny Wieser: UC Berkeley
Edward M. Stolper: Caltech

This paper is a non-peer reviewer pre-print submitted to EarthArXiv, which has been submitted to Volcanica for peer review.

Twitter handles: @eryhughes, @pip_liggins, @Penny_Wieser

VolFe: an open-source tool for calculating melt-vapor equilibria including silicate melt, carbon, hydrogen, sulfur, and noble gases

Ery C. Hughes[1,2,*], Philippa Liggins[3], Penny Wieser[4], Edward M. Stolper[2]
[1]Te Pū Ao GNS Science, National Isotope Centre/Avalon, Lower Hutt 5010, Aotearoa New Zealand
[2]Division of Geological and Planetary Sciences, Caltech, Pasadena, CA 91125, USA
[3]Oxford Research Software Engineering Group, University of Oxford, 1–4 Keble Road, Oxford OX1 3NP, UK
[4]Earth and Planetary Science, UC Berkeley, Berkeley, CA, USA
*e.hughes@gns.cri.nz
ECH: 0000-0002-3445-281X
PL: 0000-0003-2880-6711
PW: 0000-0002-1070-8323
EMS: 0000-0001-8008-8804
Keywords: volatiles, thermodynamic, degassing, open-source, melt, vapor

Abstract

VolFe is an open-source flexible and adaptable thermodynamic framework in Python for calculating the equilibrium composition of melt and vapor. VolFe considers basaltic through rhyolitic melts including the volatiles carbon, hydrogen, sulfur, and noble gases. VolFe models both reduced and oxidised systems due to the range of melt and vapor species included. Hence, VolFe is applicable to terrestrial (e.g., mid-ocean ridges to arcs) and extra-terrestrial (e.g., the Moon and Mars) systems. New parameterisations of "model-dependent variables" (e.g., volatile solubility functions, sulfide-saturation conditions, fugacity coefficients, etc.) can be added as new experimental studies come out, enhancing VolFe's future applicability. The main calculations currently included in VolFe are the pressure of vapor-saturation based on the dissolved volatile content of melts; open- and closed-system degassing and regassing; and an oxybarometer based on the melt sulfur content. As an example, we apply VolFe to melt inclusion and matrix glass data from the Marianas arc.

1 Introduction

The behaviour of volatile elements such as carbon (C), hydrogen (H), sulfur (S), the noble gases (He, Ar, Ne, etc.), and the halogens (Cl, Br, etc.) during magmatic and volcanic processes is important in volcanology and igneous petrology. Exsolving vapor from degassing can provide a driving force for eruptions, leading to explosive or quiescent addition of volatiles to the atmosphere that can impact climate and/or human health (e.g., Marshall et al., 2022; Stewart et al., 2021). Surrounding country rocks can be altered by an exsolved fluid phase, sometimes playing a role in ore formation (e.g., Simon and Ripley, 2011). The loss of volatiles to vapor can affect the physical properties, chemical compositions, and liquid lines of descent of magmas (e.g., Applegarth et al., 2013; Dingwell et al.,

1996). Additionally, the oxygen fugacity (f_{O2}) of the system can evolve during degassing because of the differing dominant oxidation states of volatile elements in coexisting melt and vapor (Anderson and Wright, 1972; Brounce et al., 2017; Burgisser and Scaillet, 2007; Candela, 1986; Carmichael and Ghiorso, 1986; Gaillard et al., 2015, 2011; Kelley and Cottrell, 2012; Métrich et al., 2009; Moussallam et al., 2014, 2016).

Quantitative understanding of volatile degassing from magmas requires both studies of natural systems as well as physical and chemical models of degassing for their interpretation (e.g., Papale et al., 2022). Consequently, there has been considerable interest in developing quantitative modelling of melt-vapor chemical equilibria for silicate melt-H_2O-CO_2, resulting in a range of applicable tools: e.g., VolatileCalc (Newman and Lowenstern, 2002); MagmaSat (Ghiorso and Gualda, 2015); Solwcad (Papale et al., 2006); and VESIcal (Iacovino et al., 2021). More recently, such tools include sulfur: e.g., CHOSETTO (Moretti et al., 2003; Moretti and Papale, 2004); an unnamed model by Gaillard and others (e.g., Gaillard et al., 2011; Gaillard and Scaillet, 2014); SolEx (Witham et al., 2012); D-Compress by (Burgisser et al., 2015); Evo (Liggins et al., 2022, 2020); MAGEC (Sun and Lee, 2022; Sun and Yao, 2024); Sulfur_X (Ding et al., 2023); MELTS (Ghiorso et al., 2023); Petrolog4[1]; and our framework that we now refer to as VolFe (Hughes et al., 2022, 2024). Despite differences in their details, these tools typically calculate the equilibrium state of melt-vapor systems given a set of independent variables (e.g., vapor saturation pressures and degassing paths). These tools have been used extensively to interpret natural sample data, such as the compositions of melt inclusions (e.g., Ranta et al., 2024; Werner et al., 2020; Wieser et al., 2021), matrix glasses (e.g., Brounce et al., 2017; Lund et al., 2018; Soule et al., 2012), and/or volcanic gases (e.g., Aiuppa et al., 2022; Burton et al., 2023).

We note the distinction between individual solubility models for specific volatiles (e.g., eq. (1) and (8) for CO_2 or eq. (2) and (9) for H_2O solubility in basaltic melts in Dixon, 1997) and these tools that model systems containing multiple volatiles by combining various solubility models. For instance, VolatileCalc is a tool that includes the CO_2 and H_2O solubility models from Dixon (1997) and others. Sometimes a new study will produce both a new solubility model and a new tool: e.g., Ding et al. (2023) describe both a new solubility model for sulfur (their eq. (9) and (10) and Table 3) and a new tool called Sulfur_X for degassing calculations. Hence, sometimes these tools have their own unique solubility models and other times they incorporate models already available in the literature or both.

[1] https://petrologsoftware.com/

In this paper we describe VolFe and its implementation via a Python package for calculating melt-vapor equilibria. The name "VolFe" derives from "Volatile + Fe" to highlight the role and evolution of f_{O2} for processes involving melt-vapor equilibria. This tool was initially developed and applied to modeling the sulfur solubility minimum and maximum in silicate melt ± vapor ± sulfide ± anhydrite assemblages for basaltic systems in which the vapor was restricted to S- and O-bearing species only (i.e., no C or H present in the system; Hughes et al., 2022) and to examine the influence of sulfur and f_{O2} on the pressure of vapor-saturation in magmas (P^{v}_{sat}, Hughes et al., 2024). Although the thermodynamic modelling was fully described in these papers, significant effort has been applied to making the underlying source code more accessible to the community (with the inclusion of documentation and examples), as well as expanding the range of possible calculations that can be performed. The goal of this paper is to explain more fully the structure of the package and its capabilities, as well as the various assumptions and approximations that are used.

2 Thermodynamic framework

VolFe calculates melt-vapor equilibria at fixed conditions that can be systematically varied to create paths (e.g., *P*-*T*). Our goal is for VolFe to be user-friendly, flexible, adaptable, and to evolve over time as new thermochemical data become available and new applications are envisioned. It is written in Python and is fully open-source (available at GitHub[2]). In this paper we describe the conceptual framework behind VolFe and the types of calculations that it can currently perform. To help with implementation by potential users (including those with little or no coding experience), we provide numerous examples of usage through Jupyter Notebooks and fuller documentation via ReadTheDocs[3].

There are three parts to the VolFe framework:

(1) phases, species, and the homogeneous and heterogeneous chemical reactions within and between them (Section 3);

(2) model-dependent variables (Section 3); and

(3) calculation of the equilibrium state of the system (Section 4).

We chose a simple thermodynamic approach to construct VolFe. The state of the system is calculated by assuming that chemical equilibrium is achieved given the values of the selected independent variables, where paths can be formed by sequential steps of these calculations (e.g., degassing). Chemical equilibrium is described by: (1) a linearly-independent set of chemical reactions

[2] https://github.com/eryhughes/VolFe
[3] https://volfe.readthedocs.io/en/latest/

among species within the melt phase or the vapor phase (i.e., homogeneous equilibria), and (2) a linearly-independent set of chemical reactions between species in the melt and vapor (i.e., heterogeneous equilibria). Linearly-independent means none of these reactions can be created by adding or subtracting combinations of the other reactions. Each chemical reaction has an equilibrium constant that constrains the relative concentrations of the reactants and products at equilibrium given the independent variables.

To use this approach, we first choose the phases that might be present and the species within them. Then we choose a set of linearly-independent equilibria that relate the species within and between the different phases. We refer to this as the thermodynamic framework of the system (Section 3). The number of independent equilibria (E) required to describe the system is determined by:

$$E = N - c, \quad (1)$$

where N is the total number of species in the system (e.g., the total number of species in the melt and vapor phases) and c is the number of components required to describe possible variations in the composition of the whole system regardless of the actual speciation (Prigogine and Defay, 1954; e.g., Section 3.1). This framework is only as good as its inventory of potential phases, species, and chemical reactions (i.e., thermochemical parameters). Thus, if there are key melt or vapor species in the system of interest to a particular problem that are currently not included in VolFe (e.g., the halogens), the results from VolFe will not be appropriate unless an appropriate number of independent reactions describing their interactions in and between the melt and vapor are added to VolFe. However, the inclusion of oxidised *and* reduced species (e.g., H_2O and H_2; CO_2 and CO_{mol}, etc.: Section 3) in the melt and vapor means magmas over a wide range of oxygen fugacities can be modelled: from reduced lunar or martian basalts to oxidised arc basalts. Additionally, various combinations of volatiles allow different systems to be modelled, from terrestrial magmas with CHOS-bearing volatiles to magmas on Io with only SO-bearing volatiles.

The values of the thermochemical parameters embedded in VolFe depend on the parameterisation chosen to evaluate them at a given set of conditions, which we term "model-dependent variables" (Section 3). These variables include equilibrium constants, solubility functions, fugacity coefficients, definitions of f_{O2} buffers, etc. They are termed "model-dependent" because different parameterisations to calculate these variables are available in the literature. For instance, the absolute f_{O2} value of the Fayalite-Magnetite-Quartz (FMQ) buffer at a certain pressure (P) and temperature (T) can be calculated using the parameterisation of Frost (1991) or O'Neill (1987), etc. Hence, the FMQ buffer is a model-dependent variable. Similarly, different parameterizations for the solubility functions of H_2O, CO_2, etc. in volatile-bearing melts (e.g., Dixon, 1997; Dixon et al., 1995; Ghiorso and Gualda, 2015;

155 Iacono-Marziano et al., 2012) and of the fugacity coefficients for species in the vapor phase (e.g.,
156 Belonoshko and Saxena, 1992; Holland and Powell, 1991; Holloway, 1977; Shi and Saxena, 1992)
157 exist in the literature. In VolFe, we have included various parameterisations from the literature of
158 these model-dependent variables that can be chosen by the user when running calculations, and new
159 ones can be added as desired. For example, if the parameterisations of the solubility function for H_2
160 currently available in VolFe (Table S8) are not appropriate for a user's system of interest (either
161 because of new data or to account for their variability as a function of the major element composition
162 of the melt), a new parameterisation could be added (see example in the ReadTheDocs). The goal is to
163 make VolFe adaptable as new parameterisations become available, especially as new experiments are
164 conducted.
165
166 Finally, to calculate the state of the system at equilibrium either statically or along a particular
167 path, we require the choice of a set of independent variables whose values we specify for the
168 calculation or at each step along the path. If the relative proportions of the phases are not required
169 (e.g., at P^v_{sat}; Hughes et al., 2024), the phase rule dictates the number of independent intensive
170 variables (i.e., the variance, F) required to specify the state of the system for a given number of phases
171 (φ) and components (c) (Gibbs, 1978, 1976):
172

$$F = c + 2 - \varphi. \quad (2)$$

173
174 Alternatively, if the equilibrium proportions of the phases are required – as is the case for
175 modelling degassing – we use Duhem's theorem. This states that for a closed-system (i.e., where the
176 masses of all components remain constant), if the masses of all the components are known, the
177 equilibrium state is completely determined once the values of any two independent variables are
178 specified, and either or both variables can be intensive or extensive (e.g., Prigogine and Defay, 1954).
179 The constancy of the bulk composition of the system to apply Duhem's theorem requires mass
180 balancing all elements across all phases present in each step on any specified path.
181
182 Whether the phase rule or Duhem's theorem is the basis for the number and nature of the chosen
183 independent variables, different choices of these variables enable different types of calculations.
184 VolFe contains functions to calculate the state of the system at equilibrium given several choices of
185 the required independent variables (Section 4). These include the pressure of vapor-saturation for a
186 given volatile-bearing melt composition and T (P^v_{sat}, Section 4.1); CO_2–H_2O isobars for a given
187 volatile-free melt composition and T (Section 4.2); the composition of melt and vapor during closed-
188 and open-system re- or degassing (Section 4.3); and estimating f_{O2} from the sulfur content in the melt
189 (Section 4.4). For calculations currently available in VolFe, T is always an independent variable and
190 paths are currently isothermal. Alternative choices of the independent variables defining a calculation

can in principle be added according to the problem to be solved, allowing flexibility (possible future applications are given in Section 7).

3 Phases, species, chemical reactions, and model-dependent variables

The thermodynamic framework outlined in the previous section requires a set of linearly-independent chemical reactions that govern how the species within each individual phase interact to achieve homogeneous equilibrium and between phases to achieve heterogeneous equilibrium. The implementation of VolFe given here is essentially that described in Hughes et al. (2024b) with a few updates (Figure 1). We outline currently available parameterisations of model-dependent variables in VolFe but interested readers should check the ReadTheDocs for the most up-to-date list. The specific parameterisation for each model-dependent variable can be chosen by the user when running calculations in VolFe (Section S1.2). Tables S1–10Table S4 detail the currently implemented parameterisations for various model-dependent variables in VolFe, including the experimental conditions covered by the calibration dataset and the independent variables.

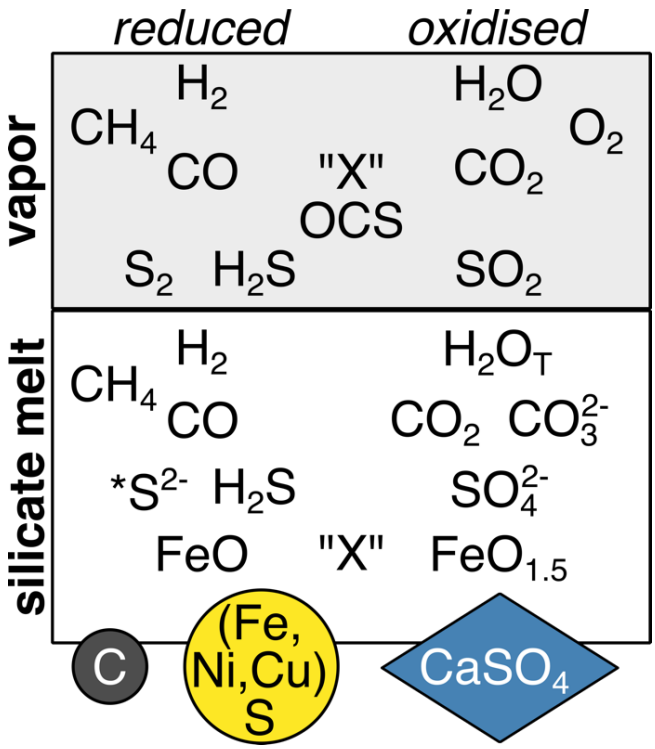

Figure 1. Phases and species considered in the thermodynamic framework of VolFe. Generally, reduced species are to the left and oxidised species are to the right. "X" represents a non-reactive molecular volatile species, such as a noble gas. Along the bottom, the small dark-grey circle represents graphite; the large yellow circle liquid sulfide; and the blue diamond anhydrite.

VolFe is primarily focused on the two-phase coexistence of melt and vapor (i.e., $\varphi = 2$). We use the term vapor throughout to describe the lower density fluid that coexists with silicate melt, although

super-critical fluid is more appropriate under certain conditions. VolFe can also test for saturation with sulfide melt, anhydrite, and/or graphite (see Section 3.5), but crystallisation of silicate or oxide minerals is not currently considered. The bulk composition of systems currently included in VolFe comprise three to six components ($3 < c < 6$): (1) a silicate component, which is defined by the volatile-free composition of the silicate melt and includes all iron as FeO (FeO_T) and all other non-volatile oxides such as SiO_2, Al_2O_3, etc. (e.g., Hughes et al., 2024, 2022); (2) the amount of oxygen (O) in excess of the silicate component (i.e., contained in the vapor, associated with volatile species in the melt, and/or associated with iron in excess of that already in the silicate component as the silicate component is defined using FeO only); and (3–6) C, H, S, and/or "X". "X" represents a non-reactive, molecular volatile species – such as a noble gas – and its chemical identity is governed by its molecular mass, fugacity coefficient, and solubility function (described in the sub-sections below). Currently "X" can be either Ar or Ne in VolFe.

The species present in the melt and vapor (Sections 3.1 and 3.2) are selected automatically by VolFe based on which volatiles are present in non-zero concentrations for the specified composition. Certain melt and vapor species can be excluded if required: e.g., treating H_2, CO, CH_4, and/or H_2S as completely insoluble in the melt or assuming these species are not present in the vapor. Such calculations allow us to evaluate the magnitude of the effects of their presence on modelled melt-vapor equilibria (e.g., Hughes et al., 2024). There are some limitations on the combinations of species possible (e.g., currently, the re/degassing calculation, cannot have both S and "X" present in the bulk composition).

3.1 Vapor

The bulk composition of the vapor phase is described by five components (C, O, H, S, and "X") and VolFe currently includes 11 chemical species in the vapor (Figure 1): O_2, H_2, CO, S_2, H_2O, CO_2, SO_2, CH_4, OCS, H_2S, and "X". Thus, based on eq. (1), the equilibrium concentrations of vapor species are related through six, linearly-independent, homogeneous vapor equilibria (i.e., $E = N - c = 11 - 5 = 6$; eq. 3–8, Table 1). Each homogenous vapor reaction has an equilibrium constant (K) that depends only on T. Currently only a single parameterisation for each K is available in VolFe from Moussallam et al. (2019), O'Neill and Mavrogenes (2022), and Ohmoto and Kerrick (1977) (further details are available in Table S1).

Table 1. Linearly-independent homogeneous vapor equilibria considered in VolFe.

Reaction among vapor species	Equilibrium constant ($K_{X(Y)}$)	Eq. no.

$H_2 + 0.5O_2 \rightleftarrows H_2O$	$K_{\mathrm{H}}(T) = \frac{f_{\mathrm{H_2O}}}{f_{\mathrm{H_2}} f_{\mathrm{O_2}}^{0.5}}$	(3)
$CO + 0.5O_2 \rightleftarrows CO_2$	$K_{\mathrm{C}}(T) = \frac{f_{\mathrm{CO_2}}}{f_{\mathrm{CO}} f_{\mathrm{O_2}}^{0.5}}$	(4)
$0.5S_2 + O_2 \rightleftarrows SO_2$	$K_{\mathrm{S}}(T) = \frac{f_{\mathrm{SO_2}}}{f_{\mathrm{S_2}}^{0.5} f_{\mathrm{O_2}}}$	(5)
$CH_4 + 2O_2 \rightleftarrows CO_2 + 2H_2O$	$K_{\mathrm{CH}}(T) = \frac{f_{\mathrm{CO_2}} f_{\mathrm{H_2O}}^2}{f_{\mathrm{CH_4}} f_{\mathrm{O_2}}^2}$	(6)
$0.5S_2 + H_2O \rightleftarrows H_2S + 0.5O_2$	$K_{\mathrm{HS}}(T) = \frac{f_{\mathrm{H_2S}} f_{\mathrm{O_2}}^{0.5}}{f_{\mathrm{S_2}}^{0.5} f_{\mathrm{H_2O}}}$	(7)
$OCS + 2CO_2 \rightleftarrows 3CO + SO_2$	$K_{\mathrm{SC}}(T) = \frac{f_{\mathrm{CO}}^3 f_{\mathrm{SO_2}}}{f_{\mathrm{CO_2}}^2 f_{\mathrm{OCS}}}$	(8)

Notes: $K_i(T)$ is the equilibrium constant and f_i is the fugacity of species i.

To implement the equilibria in Table 1 in the quantitative calculations in VolFe, we need parameterizations of all the fugacities. The partial pressure (p_i), mole fraction (x^v_i), and fugacity (f_i) for each vapor species (i) are related by:

$$p_i = \frac{f_i}{\gamma_i^v} = x_i^v P \,, \tag{9}$$

where γ_i^v is the fugacity coefficient. We treat the vapor as an ideal mixture of non-ideal gases (i.e., the Lewis-Randall rule). Given this approximation, the γ_i^v of each vapor species depends on P and T but not on the vapor composition. Currently available parameterisations in VolFe of γ_i^v are from Shaw and Wones (1964), Shi and Saxena (1992) (including modifications described in Hughes et al. 2024, 2022), and Holland and Powell (1991) (Table S2). Additionally, any vapor species can be treated as ideal (i.e., $\gamma_i^v = 1$).

At equilibrium, the sum of the partial pressures of all the vapor species equals the total pressure of the system:

$$P = \sum_{i=1}^{n} p_i = P_{\mathrm{sat}}^v. \tag{10}$$

3.2 Volatile solubility

The whole system (i.e., melt and vapor) can be described by six components (c = 6; C, O, H, S, "X", plus the volatile-free silicate component in which all Fe is present as FeO). VolFe currently includes ten volatile-bearing chemical species in the melt (Figure 1):

1. molecular H_2 ($H_{2,mol}$; e.g., Gaillard et al., 2003; Hirschmann et al., 2012; Kadik et al., 2004; Mysen et al., 2011);
2. H_2O_T (all oxidised hydrogen; e.g., Hughes et al., 2024b; Stolper, 1982);
3. molecular CO (CO_{mol}; e.g., Armstrong et al., 2015; Brooker et al., 1999; Yoshioka et al., 2019);
4. carbonate ions (CO_3^{2-}; e.g., Blank and Brooker, 1994; Dixon et al., 1995; Stolper and Holloway, 1988a);
5. molecular CO_2 ($CO_{2,mol}$; e.g., Blank et al., 1993; Blank and Brooker, 1994; Botcharnikov et al., 2006);
6. molecular CH_4 ($CH_{4,mol}$; e.g., (Ardia et al., 2013; Mysen, 2013);
7. sulfide ions other than H_2S ($*S^{2-}$; e.g., Fincham and Richardson, 1954; Klimm et al., 2012a; Métrich et al., 2009; O'Neill and Mavrogenes, 2002; Paris et al., 2001; Wilke et al., 2011; where $*S^{2-}$ refers to all S^{2-} anions in the melt not complexed with H, such as FeS, MgS, Na_2S, etc. as in Hughes et al., 2024b, 2022);
8. sulfate ions (SO_4^{2-}: e.g., Fincham and Richardson, 1954; Klimm et al., 2012b, 2012a; Métrich et al., 2009; O'Neill and Mavrogenes, 2022; Paris et al., 2001; Wilke et al., 2011);
9. molecular H_2S (H_2S_{mol}: e.g., Clemente et al., 2004; Klimm et al., 2012b, 2012a; Lesne et al., 2015); and
10. an inert molecular element ("X"$_{mol}$).

Additionally, there are the volatile-free silicate melt end-members in which all Fe is present as FeO and $FeO_{1.5}$ (shown in Figure 1 as "FeO" and "$FeO_{1.5}$"). There are thus up to 11 vapor species, ten volatile-bearing melt species, and two non-volatile-bearing melt species in the system (N = 23) and E = 23 – 6 = 17 (eq. 1). Hence, eleven linearly-independent chemical equilibria among the species are required to specify fully the equilibrium state of the system in addition to the six homogeneous equilibria among vapor species given in Table 1.

We choose nine of the additional linearly-independent reactions as heterogeneous melt-vapor equilibria describing volatile solubility in the melt. These are listed in Table 2 and derived in full in the Supplementary Material of Hughes et al. (2024). For H_2, CO, CH_4, H_2S, and "X", we assume they dissolve in the melt as the same molecular species they are present as in the vapor (eq. 12, 14, 16, 19,

and 20). For vapor species that dissolve as multiple melt species (e.g., S_2, CO_2, H_2O), the same number of linearly-independent homogeneous or heterogeneous equilibria as melt species are required (e.g., Stolper et al., 1987). For $*S^{2-}$ and SO_4^{2-}, we assume they are formed by reaction with the silicate-dominated molecular framework of the melt via the reactions given in eq. (17) and (18). In this case, each dissolved melt species has its own heterogeneous melt-vapor equilibria. However, we could have chosen the heterogeneous melt-vapor equilibria that coverts between $*S^{2-}$ and SO_4^{2-}:

$$*S^{2-}(m) + 2O_2(v) = SO_4^{2-}(m); \quad (11)$$

instead of either eq. (17) and (18), which is simply eq. (17) + (18) (e.g., Baumgartner et al., 2017; Jugo et al., 2010; Matthews et al., 1999; Métrich et al., 2009; Moretti, 2021; Moretti and Ottonello, 2005; Wallace and Carmichael, 1994). This is an example of different choices of linearly-dependent equations.

Table 2. Linearly-independent heterogeneous melt-vapor equilibria considered in VolFe.

Solubility mechanism	Solubility function	Reference for solubility mechanism	Eq. no.
$H_2(v) \rightleftarrows H_{2,mol}(m)$	$f_{H_2} = \frac{w^m_{H_{2,mol}}}{C_{H_{2,mol}}}$	Gaillard et al. (2003), Hirschmann et al. (2012), Kadik et al. (2004), Mysen et al. (2011)	(12)
$H_2O(v) \rightleftarrows H_2O_T(m)$	$f_{H_2O} \approx \frac{\left(x^m_{H_2O_T}\right)^2}{C_{H_2O_T}}$	Burnham (1979), Ghiorso and Gualda (2015), Stolper (1982a)	(13)
$CO(v) \rightleftarrows CO_{mol}(m)$	$f_{CO} = \frac{w^m_{CO_{mol}}}{C_{CO_{mol}}}$	Armstrong et al. (2015), Brooker et al. (1999), Yoshioka et al. (2019)	(14)
$CO_2(v) \rightleftarrows CO_{2,T}(m)$	$f_{CO_2} = \frac{x^m_{CO_{2,T}}}{C_{CO_{2,T}}}$	Blank et al. (1993), Blank and Brooker (1994), Botcharnikov et al. (2006), Dixon et al. (1995), Stolper and Holloway (1988b)	(15)
$CH_4(v) \rightleftarrows CH_{4,mol}(m)$	$f_{CH_4} = \frac{w^m_{CH_{4,mol}}}{C_{CH_{4,mol}}}$	Ardia et al. (2013), Mysen (2013)	(16)
$0.5S_2(v) + O^{2-}(m) \rightleftarrows *S^{2-}(m) + 0.5O_2(v)$	$f_{S_2} = \left(\frac{w^m_{*S^{2-}}}{C_{*S^{2-}}}\right)^2 f_{O_2}$	Baker and Moretti (2011), Baumgartner et al. (2017), Fincham and Richardson (1954), Gaillard et al. (2015, 2013, 2011), Gaillard and Scaillet (2014, 2009), Moretti (2021),	(17)

		Moretti and Ottonello (2003, 2005), Moretti and Papale (2004)	
$0.5S_2(v) + 1.5O_2(v) + O^{2-}(m) \rightleftarrows SO_4^{2-}(m)$	$f_{S_2} = \left(\frac{w^m_{SO_4^{2-}}}{C_{SO_4^{2-}}}\right)^2 f_{O_2}^{-3}$	Baker and Moretti (2011), Fincham and Richardson (1954), Moretti (2021), Moretti and Ottonello (2005, 2003), Moretti and Papale (2004)	(18)
$H_2S(v) \rightleftarrows H_2S_{mol}(m)$	$f_{H_2S} = \frac{w^m_{H_2S_{mol}}}{C_{H_2S_{mol}}}$	Clemente et al. (2004), Klimm et al. (2012b, 2012a), Lesne et al. (2015)	(19)
"X"(v) ⇄ "X"(m)	$f_{"X"} = \frac{w^m_{"X"}}{C_{"X"}}$	–	(20)

Notes: v = vapor; m = melt; mol = molecular; f_i = fugacity of species i; x^m_i = mole fraction or w^m_i = concentration (depending on the units) of species i in the melt; C_i = the solubility of species i, which is the constant of proportionality between the fugacity(ies) and the mole fraction/concentration of species i in the melt; $*S^{2-}$ = sulfide associated with cations in the silicate melt, rather than associated with H, i.e., H_2S_{mol}. The units of the solubility functions for H_2, CO, CH_4, H_2S, and "X" use ppm by weight (ppmw) in the melt for concentration and bars for the fugacity in the vapor. The solubility functions for H_2O_T and $CO_{2,T}$ relate the mole fraction of H_2O_T or $CO_{2,T}$ in the melt to the fugacity of H_2O or CO_2 in the vapor in bars, respectively: $x_i^m = (w_i^m/M_i)/\left(\left(w^m_{CO_{2,T}}/M_{CO_2}\right) + \left(w^m_{H_2O_T}/M_{H_2O}\right) + \left((1 - w^m_{CO_{2,T}} - w^m_{H_2O_T})/M_m\right)\right)$, where w_i^m is the weight fraction of species i in the melt; and M_i is the molecular mass of species i. The molecular mass of the melt (M_m) is of the volatile-free silicate melt composition on a single-oxygen basis as described in Dixon et al. (1995).

Water is known to dissolve in silicate melt as both molecular H_2O (H_2O_{mol}) and hydroxyl ions (OH^-) (e.g., Burnham and Davis, 1974; Dixon et al., 1995; Lesne et al., 2011; Mysen et al., 1980; Stolper, 1982b). However, as in Hughes et al. (2024), we use Sievert's law as an approximation for the solubility of H_2O in the melt (i.e., eq. 13). This states that f_{H2O} is proportional to the square of the concentration of all H dissolved as oxidised species (H_2O_T), which is the combination of OH^- and H_2O_{mol}. This would strictly apply when OH^- is the only dissolved hydrous species and there is no H_2O_{mol} (i.e., as $H_2O_T \rightarrow 0$). However, Sievert's law is a convenient and widely-used approximation where both OH^- and H_2O_{mol} species are present and is appropriate up to ~6.4 wt% H_2O_T (e.g., Burnham, 1979; Ghiorso and Gualda, 2015; Stolper, 1982). This treatment means that there is in effect only a single melt species to consider for H_2O rather than two, and therefore only a single melt-vapor equilibria is required (i.e., eq. 13). If the effects of water speciation were of specific interest, VolFe could be modified in future versions to include explicitly both H_2O_{mol} and OH^- as melt species (e.g., Dixon et al., 1995; Silver and Stolper, 1989). This would add one additional melt species and therefore would require one additional independent statement of equilibrium.

Depending on the silicate melt composition, CO_2 can dissolve dominantly as CO_2 molecules ($CO_{2,mol}$) and/or as carbonate ions (CO_3^{2-}) formed by reaction with the silicate-dominated molecular framework of the melt (e.g., Behrens et al., 2004; Botcharnikov et al., 2006; Brooker et al., 1999; Fine and Stolper, 1986, 1985). Hence, two linearly-independent equilibria involving $CO_{2,mol}$ and CO_3^{2-} are required. As described for S_2, two individual melt-vapor equilibria describing the solubility of $CO_{2,mol}$ and CO_3^{2-} could be used:

$$CO_2(v) = CO_{2,mol}(m), \quad (21)$$

$$CO_2(v) + O^{2-}(m) = CO_3^{2-}(m). \quad (22)$$

However, the total amount of carbon dissolved as oxidised species (i.e., $CO_{2,T} = CO_{2,mol}$ and CO_3^{2-}) in any given melt composition is approximately proportional to f_{CO2} regardless of the proportions of $CO_{2,mol}$ and CO_3^{2-} in the melt (e.g., Stolper et al., 1987; full derivation in the Supplementary Material of Hughes et al., 2024b). Hence, we have chosen to use only a single heterogeneous melt-vapor equilibrium in VolFe (eq. 15 in Table 2). In this case, the solubility function can be viewed as simply the sum of the solubility functions for $CO_{2,mol}$ and CO_3^{2-} (Hughes et al., 2024). To subsequently speciate $CO_{2,T}$ in the melt and calculate the concentrations of $CO_{2,mol}$ and CO_3^{2-} using VolFe, we need a second linearly-independent equilibria. Hence, we consider a homogeneous melt equilibria between $CO_{2,mol}$ and CO_3^{2-} to speciate $CO_{2,T}$ in the melt (e.g., Botcharnikov et al., 2006; Stolper et al., 1987):

$$CO_{2,mol}(m) + O^{2-}(m) \rightleftarrows CO_3^{2-}(m). \quad (23)$$

In many cases we are interested in sub-systems of the full system illustrated in Figure 1, in which case the number of linearly-independent equilibria reduces. For example, suppose the system of interest contained negligible sulfur. Then we could remove all the sulfur-bearing species (seven; Figure 1) reducing the total number of species to 15; the number of system components from six to five; and the total number of linearly-independent equations to ten. This is done automatically in VolFe if the volatile concentration of a particular component is set to 0.

3.3 Solubility functions and their dependence on *P*, *T*, and melt composition

Equations (12–20) in Table 2 describe the solubility of volatile species in the vapor-saturated silicate melt; i.e., given the fugacities of one or more vapor species and a "solubility function" for each of the *i* melt species of interest (C_i), the concentration of such melt species can be calculated (w_i^m). The formulation and parameterisation of the solubility functions in Table 2 as functions of *P*, *T*, and melt composition are key variables for the quantification of melt-vapor equilibria using VolFe. As

in Hughes et al. (2024), we use the broad term "solubility function" rather than the thermodynamically rigorous "equilibrium constant". If we used equilibrium constant, it would depend only on P and T as it is formally independent of melt composition.

As an example, we consider how the equilibrium constant for dissolving H_2 from the vapor into the melt ($K_{H2,mol}$) is derived from the corresponding solubility mechanism (eq. 12):

$$K_{\mathrm{H_{2,mol}}}(P,T) = \frac{a^m_{\mathrm{H_{2,mol}}}}{f_{\mathrm{H_2}}} = \frac{\gamma^m_{\mathrm{H_{2,mol}}} w^m_{\mathrm{H_{2,mol}}}}{f_{\mathrm{H_2}}}, \tag{24}$$

where $a^m_{\mathrm{H_{2,mol}}}$ is the activity of the H_2 species the melt; $\gamma^m_{\mathrm{H_{2,mol}}}$ is the activity coefficient of species H_2 in the melt, $w^m_{\mathrm{H_{2,mol}}}$ is the concentration (as weight fraction) of the H_2 species in the melt, and $f_{\mathrm{H_2}}$ is the fugacity of H_2 fixed by the coexisting vapor. One option is that the overall effects of melt composition are incorporated into the $\gamma^m_{\mathrm{H_{2,mol}}}(P,T,X)$ function and thus also into the solubility function:

$$C_{\mathrm{H_{2,mol}}}(P,T,X) = \frac{K_{\mathrm{H_{2,mol}}}(P,T)}{\gamma^m_{\mathrm{H_{2,mol}}}(P,T,X)} = \frac{w^m_{\mathrm{H_{2,mol}}}}{f_{\mathrm{H_2}}}, \tag{25}$$

where C_i is the solubility function and the X refers to melt composition. Alternatively, C_i is treated as a capacity, as is commonly used for sulfide and sulfate, and is the concentration-weighted sum of K_i's for each component (e.g., Fincham and Richardson, 1954; O'Neill, 2021; Spera and Bergman, 1980):

$$\begin{aligned} C_{\mathrm{H_{2,mol}}}(P,T,X) &= \sum_{i=0}^{n} w_i^m \cdot K^i_{\mathrm{H_{2,mol}}}(P,T) \\ &= w^m_{\mathrm{CaO}} \cdot K^{\mathrm{CaO}}_{\mathrm{H_{2,mol}}}(P,T) + w^m_{\mathrm{FeO}} \cdot K^{\mathrm{FeO}}_{\mathrm{H_{2,mol}}}(P,T) + etc., \end{aligned} \tag{25}$$

where i is a melt component.

The key point about using this approach is that the dependence of volatile solubility on P, T, and melt composition can be parameterized relatively straightforwardly given sufficient experimental data on the solubility of each volatile species as a function of melt composition. However, there is no universal functional form for the solubility functions in VolFe. In some cases, they are assumed to be constant (i.e., independent of P, T, and/or melt composition); a linear combinations of oxide concentrations; or vary as functions of composition based on thermodynamic constraints or alternative empirical formulation. A variety of parameterisations for the solubility functions in terms of P, T, and

397 *X* are available in the current version of VolFe. These are based on the literature and in a few cases
398 new parameterizations described in the Supplementary Material (a full list is given in Tables S3–8).
399 Additional parameterisations can be added as new experimental data and parameterisations become
400 available for all species (an example of this is shown in the ReadTheDocs).
401
402 Of particular importance for all models of volatile solubility and degassing is the strong
403 dependence of the solubility of CO_2 (i.e., $CO_{2,T}$) on melt composition (e.g., Blank and Brooker, 1994;
404 Shishkina et al., 2014; Wieser et al., 2022a). Parameterisations of $CO_{2,T}$ solubility currently available
405 in VolFe from the literature (see full list in Table S3) are typically valid over a narrow range of melt
406 composition, ranging from MORB through to alkali-rich compositions such as leucitite (Allison et al.,
407 2022, 2019; Dixon, 1997; Dixon et al., 1995; Holloway and Blank, 1994; Lesne et al., 2011a; Thibault
408 and Holloway, 1994), and for rhyolite (Blank et al., 1993). To then speciate $CO_{2,T}$ as $CO_{2,mol}$ and
409 CO_3^{2-} in VolFe, current options for the equilibrium constant for eq. (23) are for basalt (all CO_3^{2-}),
410 andesite or dacite (both CO_3^{2-} and $CO_{2,mol}$; Botcharnikov et al., 2006), and rhyolite (all $CO_{2,mol}$) (Table
411 S4). Note that currently, the effect of H_2O on CO_2 solubility is not included (e.g., Iacono-Marziano et
412 al., 2012b; King and Holloway, 2002; Papale et al., 2006). This could be implemented in the future by
413 including H_2O in the parameterisation of the CO_2 solubility function or adding an additional reaction
414 among melt species (e.g., $H_2O(m) + CO_2(m) = H_2CO_3(m)$).
415
416 The solubility function for H_2O_T is far less dependent on melt composition than $CO_{2,T}$ (e.g.,
417 Allison et al., 2022; Iacono-Marziano et al., 2012; Lesne et al., 2011; Moore et al., 1998). Currently in
418 VolFe, there are representative values for basalt (Hughes et al., 2024, using data from the compilation
419 of Allison et al., 2022) and rhyolite (derived in Supplementary Material Section S1.1 and Figure S1
420 using data from Blank et al., 1993; Kadik et al., 1972; Silver et al., 1990) (Table S5).
421
422 There are few experimental data for the solubility of CO, CH_4, and H_2 in natural silicate melt
423 compositions. Parameterisations currently available in VolFe are for basalt and andesite for H_2
424 (Hughes et al., 2024b, using data from Hirschmann et al., 2012); basalt for CO (Hughes et al., 2024b,
425 using data from Armstrong et al., 2015; Stanley et al., 2014; Wetzel et al., 2013), and basalt for CH_4
426 (Ardia et al., 2013) (Table S8).
427
428 There is a wealth of experimental data that have been used to parameterize the solubility functions
429 (often called capacities) for $*S^{2-}$ (Boulliung and Wood, 2023; O'Neill, 2021) and SO_4^{2-} (Boulliung
430 and Wood, 2023a, 2023b, 2022; O'Neill and Mavrogenes, 2022), which have been included in VolFe
431 (Table S6–7). These cover a wide range of melt compositions (basalts through rhyolite) and *T*, but not
432 *P* (although some parameterisations include a *P* dependence). For the H_2S solubility function in

VolFe, parameterisations are given in Hughes et al. (2024b) for basalt and basaltic andesite based on data from Lesne et al. (2015) and Moune et al. (2009) (Table S8).

Parameterisations for the solubility functions for inert atomic species are included in VolFe for Ar and Ne in basalt or rhyolite using data from Iacono-Marziano et al. (2010) (Supplementary Material Section S1.1, Figure S2, and Table S8).

3.4 Treatment of f_{O2}, Fe^{3+}/Fe_T, and total oxygen content

The final linearly-independent equilibrium is one that describes equilibrium between FeO and $FeO_{1.5}$. We have chosen the following widely utilized, heterogeneous melt-vapor equilibrium for this purpose (e.g., Sack et al., 1981):

$$FeO(m) + 0.25O_2(v) \rightleftarrows FeO_{1.5}(m). \quad (27)$$

Several parameterisations for the relationship between f_{O2} and Fe^{3+}/Fe^{2+} in the melt covering a wide range of P, T, and melt composition are available in VolFe (Borisov et al., 2018; Kress and Carmichael, 1991; O'Neill et al., 2018; Table S9).

By including eq. (27), VolFe returns the values of f_{O2} and Fe^{3+}/Fe^{2+} of the equilibrium state of the system. For some calculations using VolFe, f_{O2} or Fe^{3+}/Fe^{2+} are taken as independent variables (e.g., determination of P^{v}_{sat} described in Section 4.1). In such cases, the bulk oxygen content of the system varies depending on the values of the independent variables. For other calculations (e.g., closed-system degassing described in Section 4.3), f_{O2} or Fe^{3+}/Fe^{2+} are dependent variables that vary with the path of the independent variables because the bulk oxygen content of the system is conserved. Currently, VolFe does not include the option to externally buffer the f_{O2} (e.g., maintain the system at ΔFMQ+1 during degassing) where the system is open to oxygen (e.g., CHOSETTO, Moretti et al., 2003; Moretti and Papale, 2004).

Note that if the value of f_{O2} is known at a given P, T, and melt composition, then all other redox ratios (e.g., Fe^{3+}/Fe^{2+}, S^{6+}/S^{2-}, etc.) and the total amount of the O component in the melt are also fixed. Hence, only one of these f_{O2}-dependent variables (f_{O2}, Fe^{3+}/Fe_T, or S^{6+}/S_T) can be chosen as an independent variable in VolFe calculations. If the user specifies more than one such f_{O2}-dependent variable as independent, a warning will be raised and VolFe will make a choice of a single independent f_{O2}-dependent variable.

3.5 Sulfide, anhydrite, and graphite

Given the conditions (P, T, f_{O2}) and compositions of the melt ± vapor, VolFe can determine whether the system is supersaturated with respect to sulfide, anhydrite, and/or graphite. This is done by comparing the $*S^{2-}$ content of the melt to the sulfide content at sulfide saturation (S^{2-}CSS, eq. 28); the S^{6+} content of the melt to the sulfate content at anhydrite saturation (S^{6+}CAS, eq. 29); and the (f_{CO2}/f_{CO}) ratio to the equilibrium constant for graphite formation (eq. 30) (Table 3). If the silicate melt is supersaturated with respect to any of these phases (i.e., eq. 28, 29, or 30 are satisfied), the calculated coexisting silicate melt and vapor compositions are metastable relative to an assemblage containing one or more of these phases. In this case, as in Hughes et al. (2022), VolFe can limit the sulfur or carbon content of the silicate melt to that at the saturation condition (i.e., set the equations in Table 3 to equalities). For graphite, this is equivalent to graphite forming, although the amount of graphite that forms is not calculated. For sulfide liquid and anhydrite, this approximates their precipitation because the non-volatile melt composition does not change in the VolFe calculation even though in reality it would (i.e., the FeO and CaO of the silicate melt should change) and the amount of the sulfide liquid and anhydrite phases are not calculated. The oxidation state of Fe and S in the system will reflect the f_{O2} but the bulk O content of the system remains unchanged if conserved in the calculation (i.e., if anhydrite "forms", which includes O, the O content of the system does not change). This is a limitation in VolFe that could be addressed in future versions.

Table 3. Saturation conditions for sulfide, anhydrite, and graphite.

Phase	Saturation condition	Eq. no.
Sulfide	$S^{2-}\text{CSS} \leq w^m_{*S^{2-}}$	(28)
Anhydrite	$S^{6+}\text{CAS} \leq w^m_{S^{6+}}$	(29)
Graphite	$C_G(s) + O_2(v) = CO_2(v)$ $K_G = \frac{a_G f_{O_2}}{f_{CO_2}}$ $K_G \geq \frac{f_{CO_2}}{f_{CO}}$	(30)

Notes: S^{2-}CSS = sulfide content at sulfide saturation; S^{6+}CAS = sulfate content at anhydrite saturation; w^m_i = weight fraction in the melt of species i; f_i = fugacity of species i; a_i = activity of species i; K = equilibrium constant; G = graphite.

For graphite, the parameterisation of the equilibrium constant from Holloway et al. (1992) is available in VolFe (Table S10). For the S^{2-}CSS, VolFe assumes the sulfide liquid phase is pure FeS unless concentrations of Fe, Cu and/or Ni in the sulfide are specified by the user. There are multiple different parameterisations from the literature available in VolFe that cover a wide range of P, T, and

melt compositions for the S^{2-}CSS (Fortin et al., 2015; Liu et al., 2021, 2007; O'Neill, 2021; O'Neill and Mavrogenes, 2022; Smythe et al., 2017) and S^{6+}CAS (Chowdhury and Dasgupta, 2019; Zajacz and Tsay, 2019), including using PySulfSat (Wieser and Gleeson, 2023) for their calculation (Table S10).

4 Calculation of the equilibrium state of the system

Given the thermodynamic framework and model-dependent variables (Section 3), VolFe calculates the equilibrium state of the system given the choice of independent variables (see Section 2 for a discussion of the phase rule, Duhem's theorem, and the number of independent variables required for a calculation). As emphasized throughout, different calculation types are possible by choosing different independent variables. In the current implementation of VolFe, temperature is always one of the independent variables and is set by the user. Here we outline the three main types of calculations to which we have been applying VolFe (e.g., Hughes et al., 2024b, 2022), as well as some additional potentially interesting calculations. All these calculations are currently addressable using functions built into VolFe as illustrated in Figure 2. Details of exactly how to implement the calculations and worked examples are given in the ReadTheDocs.

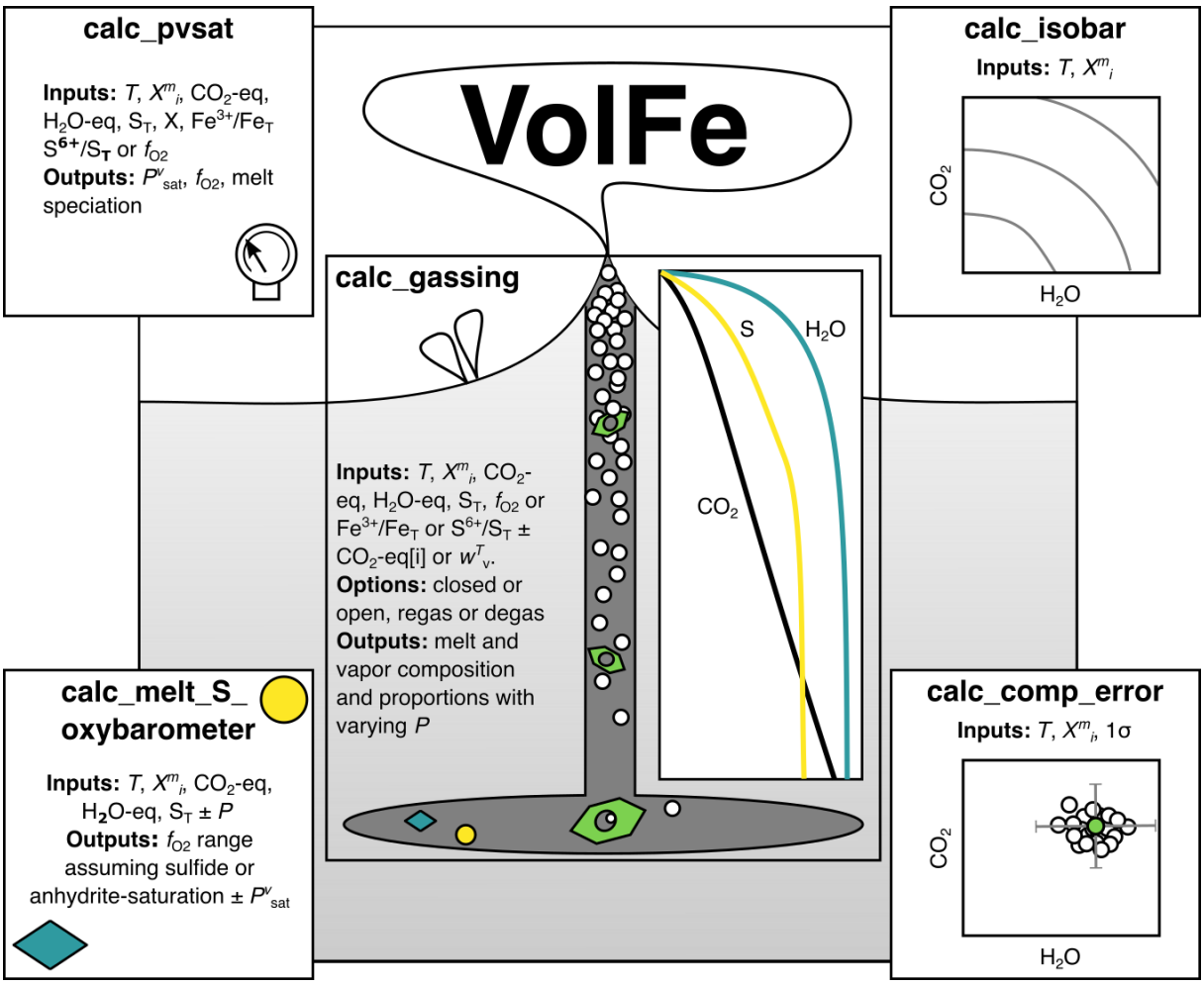

Figure 2. Schematic figure showing the key functions in VolFe: *calc_pvsat* = calculate the pressure of vapor-saturation for a given melt composition (Section 4.1); *calc_isobar* = calculate varying H_2O-CO_2 concentrations at a given *P* (Section 4.2); *calc_gassing* = calculate isothermal open- and closed-system re- and degassing paths (Section 4.3); *calc_melt_S_oxybarometer* = calculate the f_{O2} range for a given melt composition based on the sulfur content assuming sulfide- and anhydrite-saturation (Section 4.4); and *calc_comp_error* = Monte Carlo approach to generate melt compositions within analytical error (Section 4.5). Input abbreviations are: *T* = temperature; X^m_i = volatile-free melt composition; 1σ = 1 sigma error; CO_2-eq = equivalent CO_2 concentration in the melt; H_2O-eq = equivalent H_2O concentration in the melt; S_T = total sulfur in the melt; f_{O2} = oxygen fugacity of the melt; Fe^{3+}/Fe_T = Fe^{3+}/Fe_T of the melt; CO_2-eq[i] = equivalent CO_2 concentration in the melt initially; w^T_v = weight fraction of vapor present at the start of degassing; *P* = pressure; and X = concentration of "X" in the melt.

The required inputs for each calculation are detailed in the following subsections. Volatile concentrations are specified as the equivalent amounts of total hydrogen as H_2O (termed H_2O-eq, wt%), total carbon as CO_2 (CO_2-eq, ppmw), and total sulfur (S_T, ppmw). The total amount of the "X" component is simply referred to as "X" (ppmw) since there is only a single melt and vapor "X"-bearing species. Additionally for the inputs, the volatile content (i.e., the absolute values of H_2O-eq, CO_2-eq, S, and "X") is maintained, whilst the volatile-free melt composition is set to 100 wt% minus the sum of the total volatiles. For instance, if the initial volatile content was 5 wt%, initial H_2O-eq was 4.5 wt%, the inputted SiO_2 content was 45 wt%, and the total for non-volatile oxides was 99 wt%, the SiO_2 content of the melt would be (45/99)*(100–5) = 43.18 wt% and the initial H_2O-eq = 4.5 wt%.

4.1 The pressure of vapor-saturation of a magma and its use as a geobarometer

The dissolved volatile contents of a melt in equilibrium with a vapor can be used as a barometer because the sum of the partial pressures of all the vapor species – P^v_{sat} – must equal the total pressure (eq. 10) (e.g., Anderson et al., 1989; Blundy and Cashman, 2008). Calculations of P^v_{sat} have been widely applied to melt inclusions to calculate magma storage depths (e.g., Black and Andrews, 2020; Camejo-Harry et al., 2019, 2018; Colman et al., 2015; Wanless et al., 2015; Wieser et al., 2021) and to sub-aqueous matrix glasses to calculate eruption depths (e.g., Belgrano et al., 2021; Coombs et al., 2006; Lund et al., 2018; Seaman et al., 2004). As the phase proportions are not required, the phase rule defines the number of independent variables required (eq. 2: $F = 2–5$ depending on the number of volatile species in the system). The independent variables used in VolFe for this calculation are T; the total concentrations of C, H, S, and/or "X" in the melt (depending on which volatiles are present in the system); and an f_{O2}-dependent variable (e.g., f_{O2}, Fe^{3+}/Fe_T, or S^{6+}/S_T). From this, P^v_{sat}, the melt speciation (i.e., concentrations of the various dissolved melt species), and the vapor composition and speciation are calculated. This calculation is outlined in detail in Hughes et al. (2024b) (Figure 3). In brief, the pressure and melt speciation are iteratively changed until the sum of the partial pressures of all the vapor species equals the total pressure (i.e., eq. 10 is satisfied).

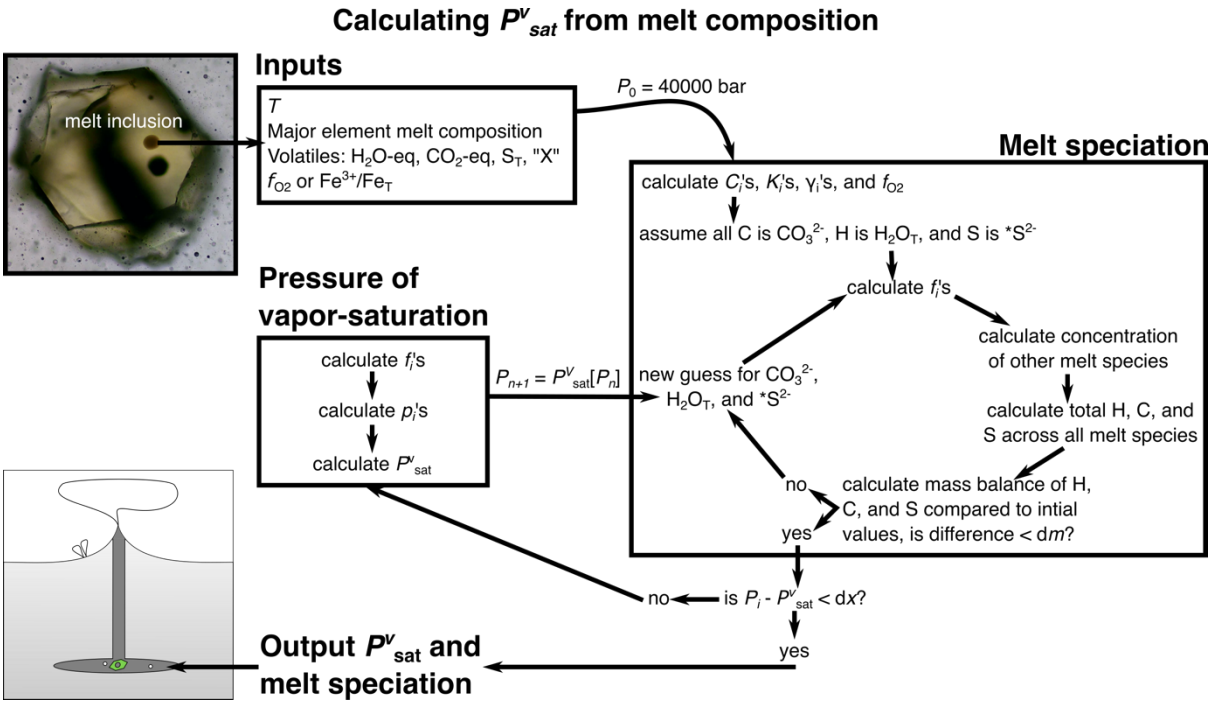

Figure 3. Flow chart describing the calculation of the pressure of vapor saturation. Adapted from the Supplementary Material of Hughes et al. (2024b). *Abbreviations:* P^v_{sat} = pressure of vapor saturation; T = temperature; H_2O-eq = equivalent amount of H as H_2O; CO_2-eq = equivalent amount of C as CO_2; S_T = total

sulfur; P_0 = initial P guess; P_n = P at iteration n; C = solubility function; K = equilibrium constant; γ = fugacity coefficient; f = fugacity; p = partial pressure; dm = mass balance tolerance; and dx = P tolerance.

4.2 Isobars

Isobars are curves or surfaces of vapor-saturated melt compositions for a fixed volatile-free base melt composition at a given P^v_{sat}. Typically, they are shown as the loci of pairs of experimentally-determined or model-calculated concentrations of H_2O_T and $CO_{2,T}$ at a single P but spanning $H_2O_T/(H_2O_T + CO_{2,T})$ from 0 to 1 in the vapor. Such diagrams have been widely used to compare the H_2O_T and $CO_{2,T}$ concentrations on these isobars to measured values in melt inclusions and matrix glasses to estimate P^v_{sat} at entrapment for melt inclusions and eruption for the matrix glasses. Such determinations are subject to a variety of caveats though (e.g., Wieser et al., 2022a).

VolFe can calculate such isobars at a given T and volatile-free melt composition assuming the melt only contains H_2O_T and $CO_{2,T}$ and the vapor only contains H_2O and CO_2. For each P, first VolFe calculates the $CO_{2,T}$ content of the melt with no H_2O_T present and the concentration of H_2O_T in the melt with no $CO_{2,T}$ present. Next, at 20 equal intervals of H_2O_T concentration in the melt between 0 and the maximum H_2O_T, VolFe calculates the associated p_{H2O}. Then, p_{CO2} is calculated from (P – p_{H2O}), and finally the $CO_{2,T}$ concentration in the melt is calculated.

4.3 Degassing and regassing paths

The main application we envision for VolFe is calculation of the compositions (including Fe^{3+}/Fe_T and therefore f_{O2}) and abundances of coexisting melt and vapor during magma degassing. For these calculations, the bulk composition of the system is specified, and P and T are the independent variables. Currently, VolFe only considers isothermal paths of vapor-saturated melt (i.e., varying P at constant T). However, many of the parameterisations of model-dependent variables have T as an independent variable so this could be adapted in the future. We refer to paths of decreasing P where vapor-saturated melt ascends as “degassing”, resulting in progressive exsolution of volatiles from melt into vapor. The reverse occurs (i.e., progressive dissolution into the melt of volatiles in the vapor) with increasing P; we refer to this as “regassing”. Regassing can happen in nature when subaerial, vesicular lava flows enter the ocean causing bubble resorption (e.g., Moore et al., 1985) or in downward limbs of a convecting bubbly magma chambers and conduit (e.g., Carey et al., 2013). The concept of regassing can also be used to reconstruct the un- or less degassed volatile contents of parental magmas. The bulk composition of the system can be varied in successive steps (e.g., by extraction or addition of vapor) to simulate open-system behaviour. Melt density can be calculated using DensityX (Iacovino and Till, 2018) in VolFe along these P-T paths.

The exact way in which the equations are solved for this by VolFe depends on the number of vapor species present but is the same for closed- and open-system re- and degassing calculations. Here, we describe briefly the calculations for a magma containing COHS-bearing volatile species (i.e., all ten vapor species, except "X"; Figure 4). Each step is solved for a given bulk composition of the system at fixed values of P and T. Given reasonable starting guesses for the mole fractions of three independent vapor species (e.g., O_2, CO, and S_2), the concentrations of all other melt and vapor species can be calculated from the homogeneous vapor and heterogeneous melt-vapor equilibria in eq. (3–8) and (12–20). Using these calculated vapor concentrations and the mass balances for C, H, O, and S across melt and vapor, we calculate the weight fraction of vapor based on each volatile element (eq. SM1–12). The values for the mole fractions of the "guessed" vapor species are then updated in successive iterations (currently using the Jacobian matrix/Newton-Raphson approach; differential equations were generated using SymPy: Meurer et al., 2017) until the difference in estimates of vapor weight fraction from each volatile element are within a specified tolerance (typically 10^{-9} weight fraction). Crucial to this approach is good initial guesses of the three vapor mole fractions at each P-step. We use values from the previous calculation step as initial guesses, which is particularly useful at the start of the degassing calculation as we can use the values at P^v_{sat} as starting guesses for the first P-step. Currently, the initial P that VolFe starts re- and degassing calculations is always the P^v_{sat} of the given melt composition (i.e., the user cannot specify the initial P). Further details of our approach are provided in Supplementary Material Section S2. Note that this specific calculation in VolFe requires using the relationship between f_{O2} and Fe^{3+}/Fe^{2+} from eq. (A-5,6) in Kress and Carmichael (1991) (i.e., the other relationships in Table S9 cannot be used currently).

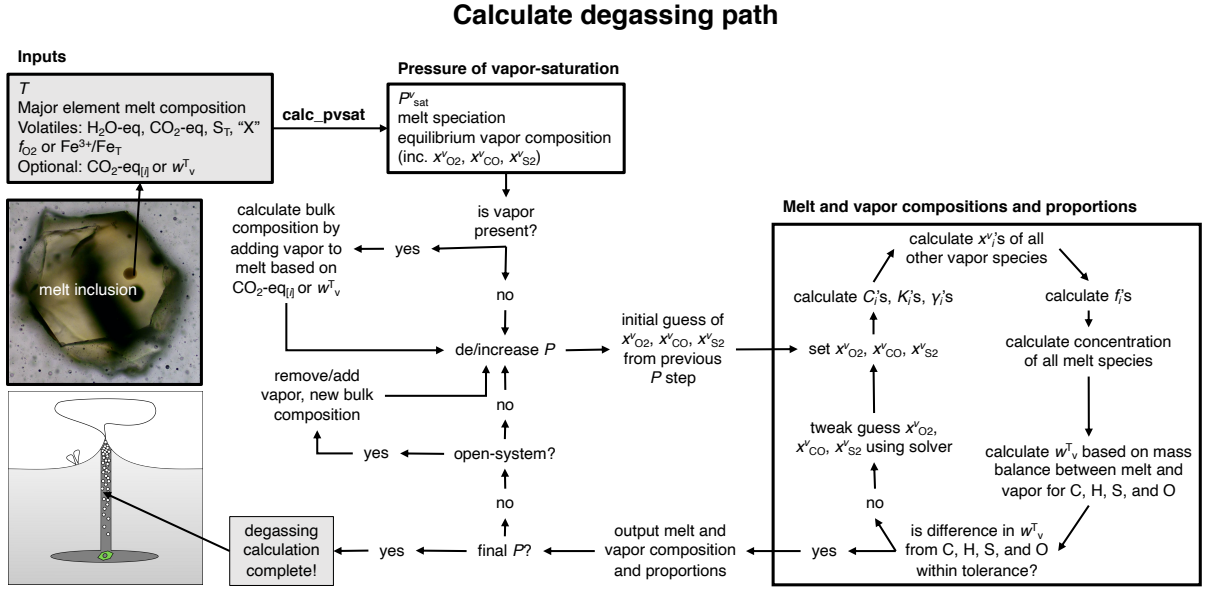

Figure 4. Flow chart describing the re/degassing calculation. *Abbreviations:* P^v_{sat} = pressure of vapor-saturation; P = pressure; T = temperature; H_2O-eq = equivalent amount of H as H_2O; CO_2-eq = equivalent amount of C as

CO_2; S_T = total sulfur; CO_2-eq$_{[i]}$ = bulk CO_2-eq concentration of the system if different to CO_2-eq; $w^T{}_v$ = weight fraction of the vapor; $x^v{}_i$ = mole fraction in the vapor; C = solubility function; K = equilibrium constant; γ = fugacity coefficient; and f = fugacity.

For closed-system calculations, the bulk composition of the system remains constant (i.e., bulk concentrations of C, O, S, H, "X", and silicate component); the melt and vapor remain in chemical equilibrium throughout; and regassing is simply the reverse of degassing. For open-system degassing, the vapor is removed at each P-step and the melt composition becomes the bulk composition of the system for the next step. For open-system regassing, a small increment of vapor that is in equilibrium with the melt is added to the system defining a new bulk composition (the amount of vapor can be user-defined). This procedure can be calculated *ad infinitum*, but in practice it would be stopped at some point defined by constraints external to the VolFe calculations (e.g., at a particular P, CO_2, H_2O, etc. content believed reasonable based on other petrological arguments – currently it stops at a user-defined P). This open-system regassing calculation is precisely analogous to correcting for fractional crystallization of olivine from a parental melt for an evolved basalt that only has olivine on its low-P liquidus. Hence, open-system regassing can be used to reconstruct the initial composition of a parental melt.

Both open- and closed re- and degassing calculations in VolFe require a T and an initial melt composition (i.e., the volatile-free melt composition, CO_2-eq, H_2O-eq, S_T and/or "X", and f_{O2} value or measured Fe^{3+}/Fe_T or S^{6+}/S_T) from which to start the calculation. For a glassy pillow rim from the sea floor, the required melt composition could simply be taken as the measured glass composition. For a melt inclusion, the required melt composition could be the bulk composition of the melt inclusion at the time of entrapment (i.e., correcting for vapor bubble formation, post-entrapment crystallisation, etc.; e.g., Rose-Koga et al., 2021). Regardless of how it is obtained, this melt composition equals the bulk composition of the system if there is no vapor present. This is always the starting condition for open-system re- and degassing calculations and can be the starting condition for closed-system degassing calculations.

Alternatively, this melt composition might coexist with a vapor (e.g., an ascending magma in which degassing had already begun). This must be the starting condition for closed-system regassing and could be the starting condition for closed-system degassing. If the amount of this coexisting vapor is known, this can be specified as in input in VolFe. VolFe then calculates the composition of this vapor at $P^v{}_{sat}$ given the specified melt composition (e.g., Section 4.1). The bulk composition of the system is then calculated as the weighted combination of the compositions of coexisting melt and vapor and the starting point for the calculation is a melt+vapor assemblage. However, the amount of vapor is often unknown. In such cases, it might be possible to estimate the bulk CO_2 content of the undegassed magma (e.g., Macpherson and Mattey, 1994; Moore and Bodnar, 2019). The amount of

vapor present can then be calculated given mass balance between the carbon in the melt and vapor at P^{v}_{sat} (the composition of the melt is known and the composition of the vapor is calculated as in Section 4.1) and the initial carbon (eq. S2–4). From this, the initial composition of all volatiles and O can be calculated and therefore the bulk composition of the system specified.

For closed-system calculations, the bulk composition of the system – including oxygen – is fixed. The constancy of total oxygen results in systematic variations in all dependent variables with progressive re- and degassing, because f_{O2}, Fe^{3+}/Fe_T and S^{6+}/S_T are all dependent variables. For VolFe, open-system *does not mean* the system is open only to oxygen, as would be the case if f_{O2} were fixed (e.g., buffered) externally. As with closed-system calculations, the changing composition of the system at each step results in continuous variations in f_{O2} and Fe^{3+}/Fe_T and S^{6+}/S_T because these are dependent variables.

At each *P*-step for open- or closed-system re- or degassing, the calculated equilibrium melt composition is checked for saturation with graphite, liquid sulfide, and/or anhydrite (Section 3.5). If the melt composition is supersaturated with respect to one or more of these phases, the user can specify that the carbon and/or sulfur content of the melt is capped at the value of saturation (e.g., the S^{2-} content of the melt is equal to S^{2-}CSS; Section 3.5) and the equilibrium state of the system is found at this different sulfur and/or carbon content. In this case, the "excess" S and/or C from the previous step (e.g., for sulfide supersaturation, this is the difference in S^{2-} between the metastable supersaturated melt S^{2-} content and that of sulfide-saturated melt for the same base melt composition) is sequestered for consideration after the next *P*-step. For open-system calculations, the additional C and/or S are then removed from the system at the next *P*-step. For closed-system calculations, if the S and/or C content of the melt drops below graphite, liquid sulfide, and/or anhydrite saturation at a subsequent *P*, the sequestered C and/or S are added back to the system. This treatment of supersaturation is relatively crude and involves a variety of approximations. However, given the small amounts of sulfide and/or anhydrite that are likely to precipitate for natural systems, and therefore the small change in melt composition, we feel this simplified treatment is likely to give reasonable results.

4.4 The "total melt sulfur oxybarometer" based on the sulfur contents of melts and glasses

Oxygen fugacity is a key thermodynamic parameter in magmatic systems because of its effects on the chemical and physical properties of the melt, the crystallization sequence and liquid line of descent, the speciation of magmatic gases, etc. (e.g., Carmichael and Ghiorso, 1990; Hughes et al., 2024b; Kolzenburg et al., 2018). There are many different oxybarometers available and, in certain circumstances, the sulfur content of the melt can be used to place bounds on the f_{O2} based on sulfide

liquid or anhydrite saturation (e.g., Beermann et al., 2011; Hughes et al., 2022; Muth and Wallace, 2022), which we term the "total melt sulfur oxybarometer". A short description of our approach is given here (Figure 5); see Section "Using w^m_{ST} as an oxybarometer" in Hughes et al. (2022) for a fuller description.

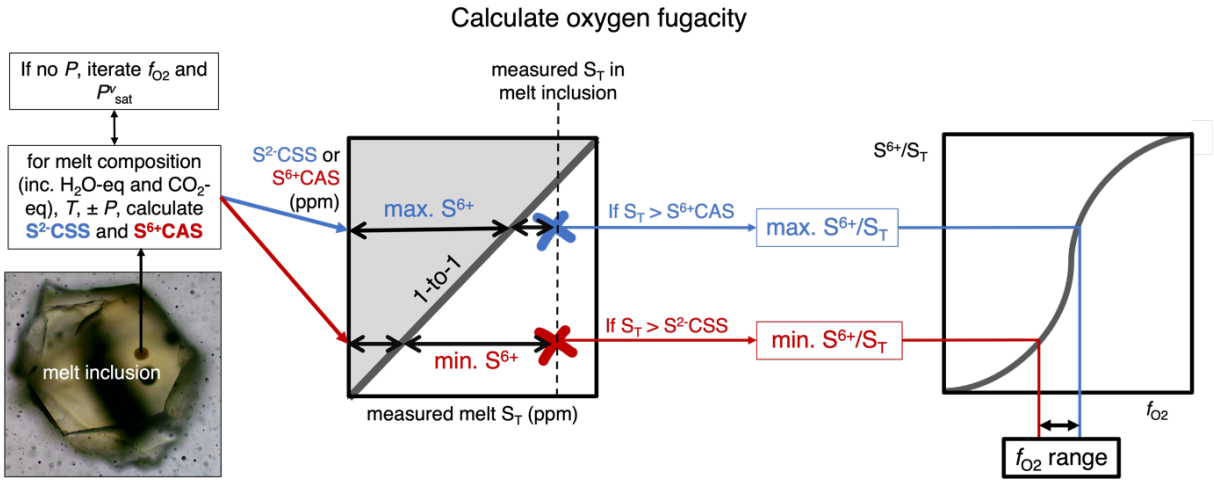

Figure 5. Schematic of how the melt sulfur content oxybarometer works. The crosses represent the measured S_T vs. calculated S^{2-}CSS and S^{6+}CAS.

The logic is the same whether using sulfide- or anhydrite-saturation as a constraint on S^{6+}/S_T and therefore f_{O2}: hence, we first describe the case for sulfide-saturation. At equilibrium, the concentration of sulfur dissolved in the melt as S^{2-} cannot exceed the S^{2-}CSS as any additional S^{2-} would go into a liquid sulfide phase. Hence, any sulfur in excess of the S^{2-}CSS must be dissolved as S^{6+}, which gives a lower bound on S^{6+}/S_T (red path in Figure 5). It provides a minimum S^{6+}/S_T because the melt might not be sulfide-saturated, in which case more of the sulfur dissolved in the melt is S^{6+} and the true S^{6+}/S_T will be higher. However, if the melt is known to be sulfide-saturated, this would then give the actual S^{6+}/S_T. If the concentration of sulfur dissolved in the melt is less than the S^{2-}CSS, no lower bound on S^{6+}/S_T is possible. Similarly, for anhydrite-saturation, the concentration of sulfur dissolved in the melt as S^{6+} cannot exceed the S^{6+}CAS as any additional S^{6+} would go into an anhydrite phase. Hence, any sulfur in excess of the S^{6+}CAS must be dissolved as S^{2-}, which gives an upper bound on S^{6+}/S_T (blue path in Figure 5). It provides a maximum S^{6+}/S_T because the melt might not be anhydrite-saturated, in which case more of the sulfur dissolved in the melt is S^{2-} and the true S^{6+}/S_T will be lower. However, if the melt is known to be anhydrite-saturated, this would then give the actual S^{6+}/S_T. If the concentration of sulfur dissolved in the melt is less than the S^{6+}CAS, no upper bound on S^{6+}/S_T is possible.

For both sulfide- and anhydrite-saturation, the S^{6+}/S_T can then be converted to an f_{O2} using eq. (11). Hence, if the sulfur content is high enough, for a given T, volatile-free melt composition, and

volatile content, a range of allowable f_{O2} values can be calculated using VolFe (Figure 5). Either P can be specified or the calculation can be done assuming vapor-saturation such that the calculated P is P^{v}_{sat}. If the specified P is too low for the given volatile content, the melt will be vapor-supersaturated and hence metastable.

In VolFe, this is implemented by calculating the S^{2-}CSS and S^{6+}CAS for the given conditions (T, P, and melt composition including volatiles). VolFe then compares the S^{2-}CSS and S^{6+}CAS to the measured sulfur content (S_T). If $S_T > S^{2-}$CSS or S^{6+}CAS, it calculates $S^{6+}/S_T = (S_T - S^{2-}CSS)/S_T$ or $(S_T - S^{6+}CAS)/S_T$ and then converts it to f_{O2}. If $S_T < S^{2-}$CSS or S^{6+}CAS, it cannot calculate a minimum or maximum f_{O2}, respectively. If the calculation is at P^{v}_{sat}, VolFe iteratively calculates P and f_{O2} until convergence.

4.5 Monte Carlo errors for melt composition

Inputs to all these calculations (e.g., oxide concentration, volatile contents, Fe^{3+}/Fe_T, etc.) will have uncertainties associated with them and it can be useful to see how these errors influence the results. A Monte Carlo approach can be applied in VolFe to the melt composition assuming absolute or relative errors are independent and normally distributed given one standard deviation values for them. This does not constrain uncertainties introduced by model-dependent variables in VolFe (e.g., solubility functions, fugacity coefficients, etc.). These compositions can then be used as starting conditions for the calculations described in Section 4.

5 Example application to basaltic glasses from the Marianas arc

We illustrate the use of VolFe by applying the calculations described in Section 4 to data from the Marianas arc (Brounce et al., 2016, 2014; Kelley and Cottrell, 2012). These data were chosen because they have CO_2-eq, H_2O-eq, S, Fe^{3+}/Fe_T, and major element composition measured for each melt inclusion glass and matrix glass, which are required inputs for most VolFe calculations (e.g., Figure 6). This is also an opportunity to show how calculations using VolFe could be described and cited. We recommend that the original reference for the specific parameterisations of the model-dependent variables used within the VolFe calculations be clearly cited. Additionally, if the parameterisation is implemented in VolFe using an external Python package this should also be cited (e.g., S^{2-}CSS using PySulfSat by Wieser and Gleeson, 2023; melt density using DensityX by Iacovino and Till, 2018).

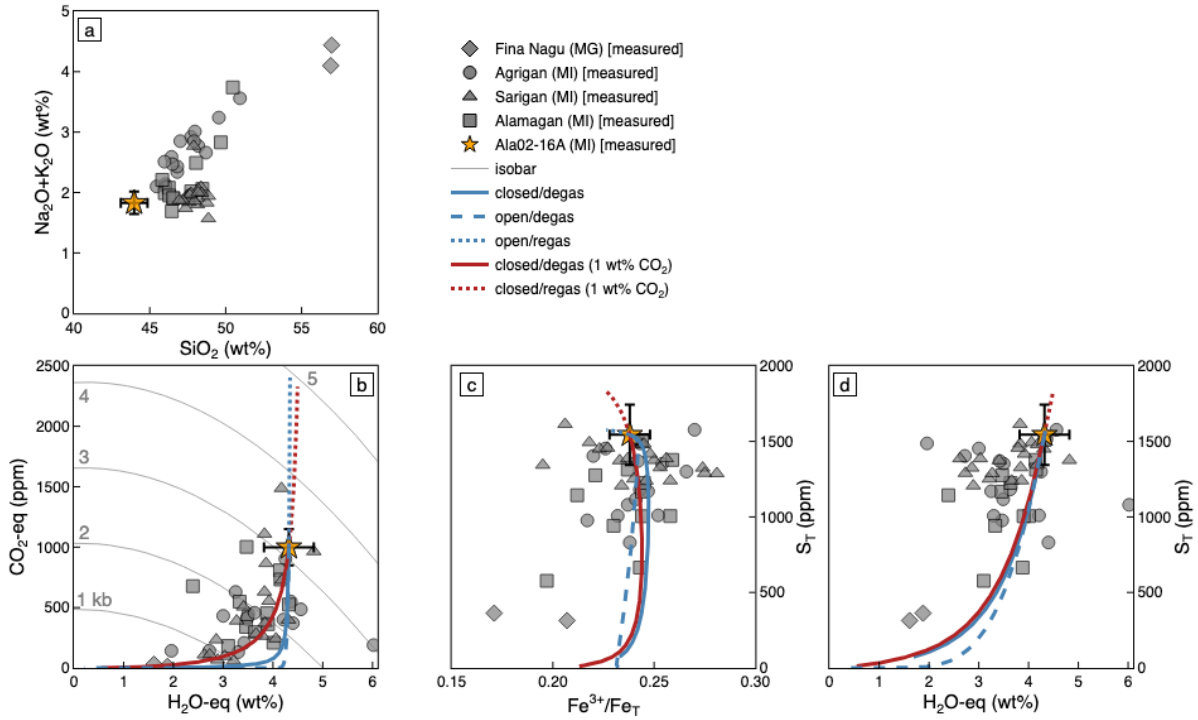

Figure 6. Measured melt inclusion (MI) and matrix glass (MG) data from the Marianas arc (Brounce et al., 2016, 2014; Kelley and Cottrell, 2012) and modelling results using VolFe: **(a)** normalised SiO_2 vs. normalised total alkalis (Na_2O+K_2O); **(b)** CO_2-eq vs. H_2O-eq; **(c)** S_T vs. Fe^{3+}/Fe_T; and **(d)** S_T vs. H_2O-eq. Symbols are measured data (grey), where the shape indicates MI or MG and volcano (diamond = Fina Nagu MG, circle = Agrigan MI, square = Sarigan MI, and triangle = Alamagan MI). The yellow star is MI Ala02-16A and the associated error bars are 2 sigma values of assumed analytical error (see text for details). Isobars (grey curves) are shown in (b) for Ala02-16A. Re- and degassing paths are shown in (b–d) starting from the composition of Ala02-16A assuming: closed-system degassing (blue solid); closed-system degassing (red solid) and regassing (red dot) with 1 wt% initial CO_2; and open-system degassing (blue dash) and regassing (blue dot).

5.1 Data and calculations

We used the measured volatile-free melt composition, H_2O-eq, CO_2-eq, S_T, and Fe^{3+}/Fe_T for olivine-hosted basaltic melt inclusions (n = 49; Arigan = circle, Sarigan = triangle, and Alamagan = square) and basaltic-andesite matrix glass data (n = 2; Fina Nagu = diamond) from the Marianas arc (Figure 6; Brounce et al., 2016, 2014; Kelley and Cottrell, 2012). The temperature for each glass composition was calculated based on the measured volatile-free melt composition and H_2O-eq using eq. (14) from Putirka (2008) as implemented in Thermobar (v1.0.41; Wieser et al., 2022). This calculated T depends on melt composition and water content, but not P. These calculated T were then used in subsequent VolFe calculations, which used VolFe v0.3. P^{v}_{sat} and f_{O2} were calculated for each glass composition using VolFe(Section 4.1). The measured S_T content was also used to calculate f_{O2} based on the total-melt-sulfur-oxybarometer assuming vapor-saturation using VolFe (Section 4.4).

To evaluate the influence of errors associated with measurements of the melt composition on calculated T, P^{v}_{sat}, and f_{O2}, we randomly generated 1000 different compositions using a Monte Carlo approach in VolFe for melt inclusionAla02-16A (yellow star in Figure 6; Section 4.5). Errors were assumed to be independent and normally distributed with the following one sigma values typical for these types of analyses: ±0.25 wt% H_2O; ±75 ppm CO_2; ±100 ppm S; ±0.005 Fe^{3+}/Fe_T; ±1% relative for major oxides; and ±5% relative for minor oxides (note that ±2 sigma errors are shown on Figure 6 for all species). Each of these 1000 compositions based on Ala02-16A was then used to calculate T, P^{v}_{sat}, and f_{O2} (but not degassing paths) as described in the previous paragraph.

We used the composition of Ala02-16A (i.e., measured volatile-free melt composition and calculated T; Fe^{3+}/Fe_T and S are not used in this calculation) to calculate isobars using VolFe for varying H_2O_T and $CO_{2,T}$ at 1000–5000 bar in 1000 bar increments (Section 4.2). We also calculated various closed- and open-system re- and degassing paths using VolFe (Section 4.3) with Ala02-16A as the starting melt composition (i.e., measured glass composition: 999 ppm CO_2-eq, 4.52 wt% H_2O-eq, 1544 S_T, 0.238 Fe^{3+}/Fe_T, volatile-free melt composition, and the calculated T of 1111 °C) assuming: (1) isothermal closed-system degassing with no vapor at the start of degassing; isothermal open-system (2) degassing and (3) regassing; and isothermal closed-system (4) degassing and (5) regassing where the bulk system contains 1 wt% CO_2 (i.e., vapor is present at the yellow star). Regassing was calculated up to 5000 bar.

For the VolFe calculations, melt species included were H_2O_T, $CO_{2,mol}$, CO_3^{2-}, $H_{2,mol}$, CO_{mol}, $CH_{4,mol}$, $*S^{2-}$, SO_4^{2-}, and H_2S_{mol}; vapor species included were O_2, CO, H_2, S_2, CO_2, H_2O, SO_2, CH_4, H_2S, and OCS. The fugacity coefficients used are from Shi and Saxena (1992) for O_2, CO, S_2, CO_2, CH_4, and OCS; Shaw and Wones (1964) for H_2; Holland and Powell (1991) for H_2O; and Shi and Saxena (1992) for SO_2 and H_2S as modified in (Hughes et al., 2022, 2024). The equilibrium constants used for homogeneous vapor equilibria are reactions c–f and h from Ohmoto and Kerrick (1977) for CO_2, H_2O, SO_2, CH_4, and H_2S; and eq. (8) from Moussallam et al. (2019) for OCS. The solubility functions used are from Hughes et al. (2024) for H_2O_T, $H_{2,mol}$, CO_{mol}, and H_2S_{mol}; Dixon et al. (1995) for $CO_{2,T}$; eq. (7a) from Ardia et al. (2013) for CH_4; eq. (10.43) from O'Neill (2021) for $*S^{2-}$; and eq. (12a) from O'Neill and Mavrogenes (2022) for SO_4^{2-}. All $CO_{2,T}$ is assumed to be CO_3^{2-} as the composition is a basalt (e.g., Fine and Stolper, 1986). Iron speciation is calculated using eq. (A-5,6) from Kress and Carmichael (1991) and the FMQ buffer is Frost (1991). The parameterisation for S^{2-} CSS uses eq. (10.34, 10.43, 10.45, 10.46, 10.49) in O'Neill (2021) assuming the sulfide is pure FeS, and S^{6+}CAS is eq. (8–14) in Zajacz and Tsay (2019). Graphite saturation uses eq. (3) in Holloway et al. (1992). [*Note:* This paragraph could be replaced by a reference to Table S11.]

5.2 Results and discussion

The Marianas arc melt inclusions and matrix glasses record temperatures from 1104–1135 °C, with melt inclusions from Agrigan volcano and matrix glasses from Fina Nagu volcanic chain having lower temperatures than melt inclusions from Alamagan and Sarigan volcanoes (Figure 7a). The calculated values of P^{v}_{sat} imply the melt inclusions were trapped at a range of pressures from 763–3753 bars, with no systematic variation with T or volcano (circles, squares, and triangles in Figure 7a and b). The two matrix glasses are calculated to have quenched at shallower pressures (296–327 bars) compared to the melt inclusions (diamonds in Figure 7a and b). The calculated f_{O2} values range from ΔFMQ+0.5 to +1.6, with no apparent systematic inter-volcano difference (Figure 7b). For melt inclusion Ala02-16A, propagation of assumed uncertainties on its measured composition result in a calculated T value of 1111 ± 3 °C, P^{v}_{sat} value of 3229 ± 158 bar, and ΔFMQ value of +1.26 ± 0.06 (yellow star in Figure 7a and b). The uncertainty on T due to melt composition uncertainty (±3 °C) is far less than the reported standard estimate of error of this thermometer (±51 °C; Putirka, 2008). This highlights that including analytical uncertainties from melt composition represents *minimum* uncertainties and does not include model error.

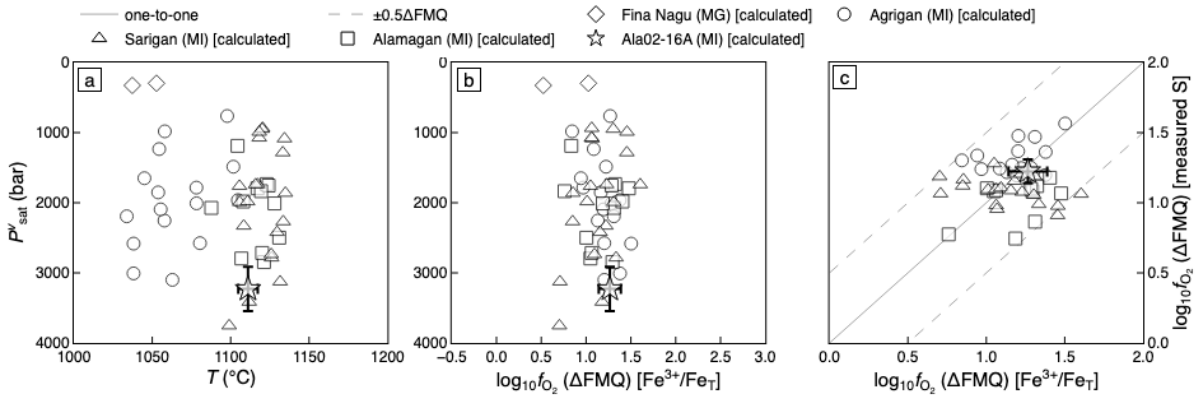

Figure 7. Results for the pressure of vapor-saturation barometer calculations using measured Fe^{3+}/Fe_T (Section 4.1) for the Marianas dataset showing calculated P^{v}_{sat} vs. **(a)** calculate T using eq. (14) from Putirka (2008) implemented in Thermobar (Wieser et al., 2022b); and **(b)** calculated ΔFMQ from Fe^{3+}/Fe_T. **(c)** Calculated ΔFMQ using measured sulfur concentration vs. calculated ΔFMQ using measured Fe^{3+}/Fe_T, where the solid line it the one-to-one relationship and dotted lines are ±0.5ΔFMQ. Symbol shape indicates MI or MG and volcano (diamond = Fina Nagu MG, circle = Agrigan MI, square = Sarigan MI, and triangle = Alamagan MI). The star is MI Ala02-16A and the associated error bars associated are 2 sigma values based on calculations using 1000 compositions generated from a Monte Carlo approach (see text for details).

As well as using the measured Fe^{3+}/Fe_T to calculate f_{O2}, we also used the total-melt-sulfur-oxybarometer (Section 4.4; Figure 7c). Only minimum estimates of f_{O2} were possible using the measured sulfur content because the sulfur contents were not high enough to be potentially saturated with anhydrite (Hughes et al., 2022). A few glasses did not have sufficient sulfur for a minimum f_{O2}

838 estimate because their sulfur contents are less than S^{2-}CSS (e.g., the two matrix glasses – grey
839 diamonds – are not shown in Figure 7c). The calculated ΔFMQ using measured Fe^{3+}/Fe_T are within
840 half a log unit of that using measured sulfur content assuming sulfide-saturation (Figure 7c).
841 However, some estimates from the total-melt sulfur-oxybarometer, which represent minimum f_{O2}
842 estimates, are higher than based on measured Fe^{3+}/Fe_T (i.e., above the one-to-one line in Figure 7c).
843 This could suggest that the melt composition is metastable with respect to sulfide saturation (although
844 sulfides are not reported in these glasses in the original studies); the S^{2-}CSS parameterisation used is
845 not accurate for these conditions (e.g., assuming the sulfide liquid is pure FeS or that a different
846 parameterisation is more appropriate); or it could be an indication of the error (e.g., on the calculated
847 S^{2-}CSS) in such calculations (e.g., Hughes et al., 2024b, 2022). For Ala02-16A, propagation of
848 assumed uncertainties on its composition result in calculated ΔFMQ value of +1.22 ± 0.04 based on
849 the total-melt-sulfur-oxybarometer, which is similar to using measured Fe^{3+}/Fe_T (+1.26 ± 0.05; yellow
850 star in Figure 7c).
851
852 Open-system degassing from Ala02-16A results in a steep decrease in CO_2-eq relative to H_2O-eq
853 (blue dash curves; Figure 6b). Closed-system degassing curves are less steep, where the steepness
854 decreases as the amount of vapor present at the start of degassing increases (blue and red solid curves;
855 Figure 6b). This highlights the high CO_2/H_2O of the vapor relative to the melt and the volatile-
856 buffering capacity of the vapor if present (e.g, Dixon and Stolper, 1995). Both the open- and closed-
857 regassing paths are similar for CO_2-eq vs. H_2O-eq up to 5000 bar (Figure 6b). Degassing paths for S_T
858 vs. H_2O-eq are concave-up highlighting that sulfur degasses slightly before H_2O-eq, with open-system
859 degassing being slightly steeper (Figure 6d). The regassing paths to P = 5000 bar go to much higher
860 CO_2-eq (Figure 6b) but not much higher S_T or H_2O-eq than the yellow star (Figures 6c and 6d). This
861 reflects that the gas being added to the melt is CO_2-rich (Figure 8b) and relatively S- and H_2O-poor
862 (Figure 8a, c, and d). Hence, a lot of CO_2-eq is added to the melt but very little S_T and H_2O-eq. The
863 regassing calculation could be used to estimate the composition and P^{v}_{sat} of permissible parental
864 liquids from which the entrapped melt inclusion glasses formed by degassing.
865
866

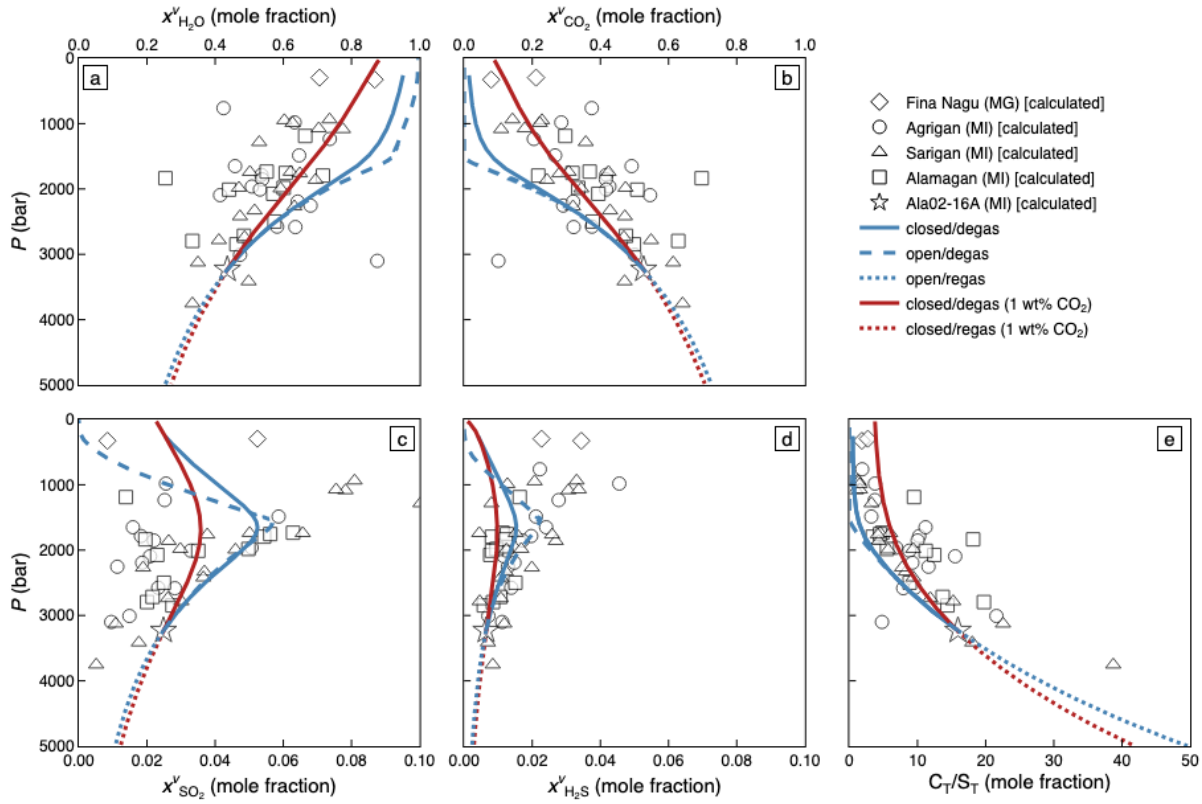

Figure 8. Vapor composition for open- and closed-system re- and degassing calculations (Section 4.3) for Ala01-16A from the Marianas dataset, showing *P* vs. mole fraction in the vapor for: **(a)** H_2O, **(b)** CO_2, **(c)** SO_2, **(d)** H_2S; and **(e)** C_T/S_T. All other vapor species (O_2, H_2, CO, S_2, CH_4, and OCS) are always <0.01. Curves begin at melt inclusion Ala01-16A (star) for: closed-system degassing assuming Ala01-16A represents the bulk composition of the system (blue solid); closed-system degassing (red solid) and regassing (red dot) assuming the bulk system has 1 wt% CO_2-eq; and open-system degassing (blue dash) and regassing (red dash). Symbols (white) show calculated vapor speciation at calculated P^v_{sat} (Section 4.1) for natural glasses for comparison with the degassing paths calculated using VolFe. The shape indicates MI or MG and volcano (diamond = Fina Nagu MG, circle = Agrigan MI, square = Sarigan MI, and triangle = Alamagan MI).

In the degassing calculations, CO_2 begins to degas first (Figure 9b). Carbon dioxide is always the dominant volatile component in the vapor exsolved early in the degassing sequence due to its low solubility (e.g., Dixon and Stolper, 1995), with water and sulfur degassing after (Figure 9a–c). Deep degassing of sulfur is related to the high water content of the melt (e.g., Ding et al., 2023; Rasmussen et al., 2020). Assuming the bulk composition contains 1 wt% CO_2 causes all volatiles to start degassing deeper than for the melt composition with ~1000 ppm CO_2-eq and this effect on S is the most notable (red vs. blue solid curves; Figure 9a–c). There is little change in Fe^{3+}/Fe_T and ΔFMQ during open- and closed-system re- and degassing (including when the bulk system contains 1 wt% CO_2-eq), suggesting the melt started near its sulfur solubility minimum (Figure 9f; e.g., Hughes et al., 2022). Below ~1000 bar, open-system degassing causes slight oxidation, whilst closed-system causes slight reduction due to the change in bulk composition of the system during open-system degassing. A similar pattern is seen in S^{6+}/S_T (Figure 9e). However, because S^{6+}/S_T is more sensitive to changes in

f_{O2} at this f_{O2} (i.e., on the steeply rising part of the sigmoid for S^{6+}/S_T vs. f_{O2}) the calculated variations in S^{6+}/S_T are larger.

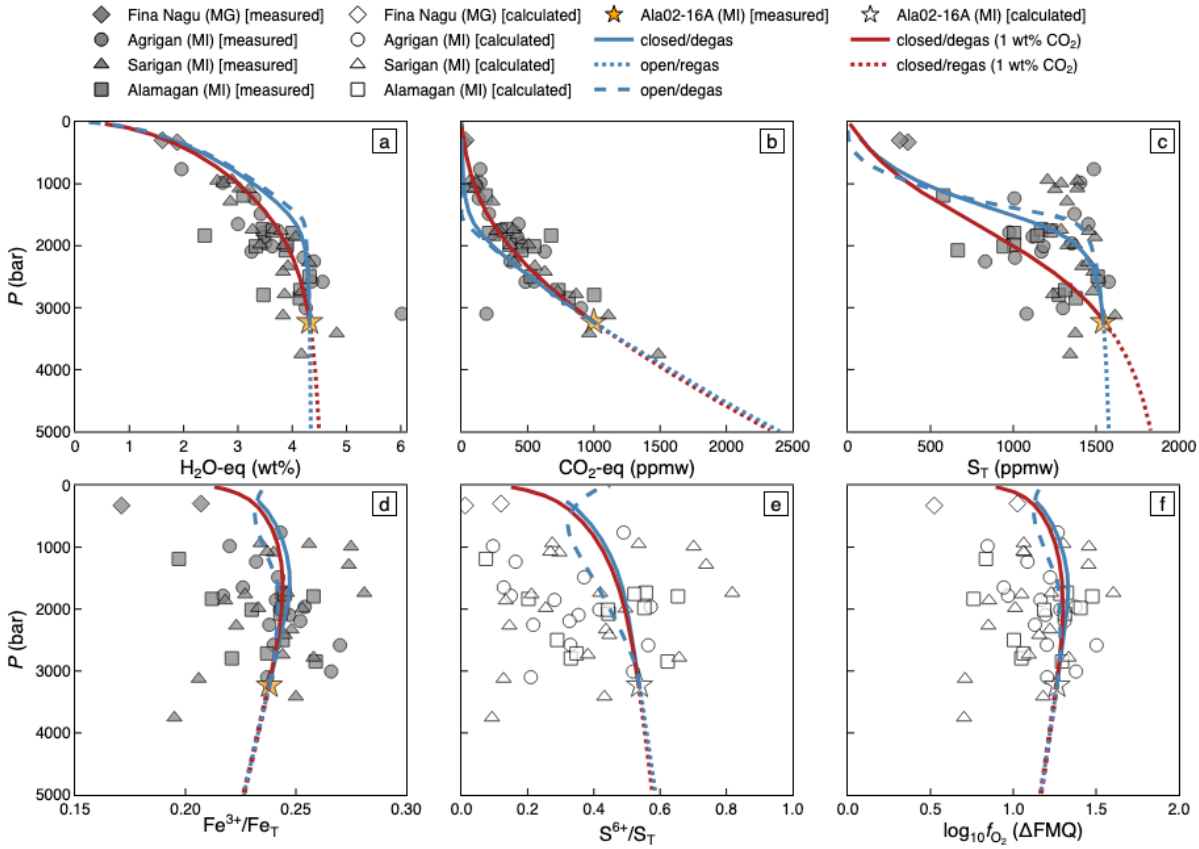

Figure 9. Melt composition for open- and closed-system re- and degassing calculations (Section 4.3) for Ala01-16A from the Marianas dataset, showing P vs. **(a)** H_2O-eq, **(b)** CO_2-eq, **(c)** S_T, **(d)** Fe^{3+}/Fe_T; **(e)** S^{6+}/S_T, and **(f)** ΔFMQ. Curves begin at melt inclusion Ala01-16A (yellow/white star) for: closed-system degassing assuming Ala01-16A represents the bulk composition of the system (blue solid); closed-system degassing (red solid) and regassing (red dot) assuming the bulk system contains 1 wt% CO_2-eq; and open-system degassing (blue dash) and regassing (red dash). Symbols show measured melt volatile contents (grey, a–d) or calculated values (white, e and f) at calculated P^{v}_{sat} (Section 4.1) for natural glasses for comparison with the degassing paths calculated using VolFe. The shape indicates MI or MG and volcano (diamond = Fina Nagu MG, circle = Agrigan MI, square = Sarigan MI, and triangle = Alamagan MI).

The vapor begins CO_2-dominated and continuously transitions to H_2O-dominated as pressure decreases, with open-system degassing stripping the vapor of CO_2 more rapidly (Figure 8a and b). SO_2 is the dominant sulfur-bearing vapor species, reflecting the relatively oxidised nature of the melt, followed by H_2S (Figure 8c and d). The mole fraction in the vapor of both these species increases then decreases with decreasing P at ~1800 bars for all degassing paths. This is in the P range in which significant degassing of sulfur and water occurs (Figure 8a and c). All other vapor species (i.e., O_2, S_2, H_2, CO, CH_4, and OCS) are <1% by mole fraction throughout degassing reflecting the oxidized bulk composition of the system. The C_T/S_T ratio in the vapor (i.e., all carbon and sulfur-bearing vapor species) decreases during degassing, where the final value reflects the initial value of the melt as

essentially all the volatiles are degassed at the surface (Figure 8e). This is often used as an indication of magma depth in volcano monitoring from plume and fumarole chemistry (e.g., Kern et al., 2022).

For comparison to the degassing paths, we plot the measured (grey symbols: CO_2-eq, H_2O-eq, S_T, and Fe^{3+}/Fe_T) or calculated at P^v_{sat} (white symbols: S^{6+}/S_T, ΔFMQ, and vapor compositions) values for the individual melt inclusion and matrix glass analyses (Figure 6, Figure 8, and Figure 9). However, the glasses come from different volcanoes and are therefore not related by simple re- and degassing processes (Brounce et al., 2016, 2014; Kelley and Cottrell, 2012). Broadly, degassing for a bulk system containing 1 wt% CO_2-eq results in similar trends to the melt inclusion and matrix glass data. This is less true for sulfur-related parameters (e.g., S_T, S^{6+}/S_T, x^v_{H2S}, and x^v_{SO2}). This is likely because the parameterisations used for the sulfide and sulfate solubility functions are highly-dependent on melt composition and T, whilst for H_2O and CO_2 these are independent or weakly-dependent on these variables. Melt composition and T are not constant for the melt inclusion and matrix glass data but are for the calculated re- and degassing paths. However, this highlights the utility of applying VolFe to natural sample data to understand melt-vapor equilibria in such systems.

6 Comparison to other approaches

As emphasized in Section 1, there are several other tools available to calculate melt-vapor chemical equilibria. These tools differ from VolFe in the volatile elements included; melt and vapor species considered; approach to formulation; parameterisations of model-dependent variables available; and types of calculations included. A full comparison of the various tools is beyond the scope of this paper, but a preliminary comparison between some tools can be found in Hughes et al. (2023), and key differences are discussed here. The models we compare to are VolatileCalc (Newman and Lowenstern, 2002), VESIcal (Iacovino et al., 2021), Solcwad (Papale et al., 2006), MagmaSat (Ghiorso and Gualda, 2015), SolEx (Witham et al., 2012), Sulfur_X (Ding et al., 2023), CHOSETTO (Moretti et al., 2003; Moretti and Papale, 2004), MELTS (Ghiorso et al., 2023), Petrolog4, DCompress (Burgisser et al., 2015), Evo (Liggins et al., 2022, 2020), and MAGEC (Sun and Lee, 2022; Sun and Yao, 2024).

- Water and CO_2 in the melt and vapor: All models consider these species.
- H_2, CO, and CH_4 in the melt and vapor: Not included in VolatileCalc VESIcal, Solcwad, MagmaSat, SolEx, Sulfur_X, CHOSETTO, MELTS, or Petrolog4. Included in DCompress, Evo, MAGEC, and VoFe.
- Sulfur-bearing species in the vapor: Not included in VolatileCalc, VESIcal, Solcwad, or MagmaSat. SolEx considers total sulfur only. Sulfur_X, CHOSETTO, MELTS, and Petrolog

consider H_2S and SO_2. Evo considers S_2, H_2S, and SO_2, whilst DCompress, Gaillard, MAGEC, and VolFe additionally consider OCS.

- Sulfur-bearing species in the melt: Not included in VolatileCalc, VESIcal, Solcwad, or MagmaSat. SolEx considers total sulfur. Sulfur_X, CHOSETTO, MELTS, Petrolog, EVo, Gaillard, and MAGEC consider S^{2-} and S^{6+}. DCompress considers H_2S and $SO_{2,mol}$. VolFe considers $*S^{2-}$, H_2S, and S^{6+}.
- Other species: Evo includes N_2 as a non-reactive species, similar to "X" in VolFe. SolEx includes Cl. MELTS includes Cl and F.
- Modelling sulfur: SolEx, Sulfur_X, and Petrolog4 use a partition coefficient approach rather than the solubility function approach on which DCompress, CHOSETTO, Evo, Gaillard, MAGEC, and VolFe are based.
- Oxygen: Sulfur_X, DCompress, Petrolog4, Evo, Gaillard, MAGEC, and VolFe are a closed-system to oxygen. CHOSETTO externally buffers the system during degassing and hence oxygen is not conserved.
- Calculation types: All these tools calculate closed-system degassing paths. Some tools calculate open-system degassing (e.g., VolatileCalc). Only VolFe calculated open- and closed regassing. Most of the tools can calculate P^{v}_{sat} (except CHOSETTO and DCompress). Some tools can calculate isobars (e.g., VolatileCalc, VESIcal, etc.). None aim to calculate melt-vapor composition for other independent variables (e.g., f_{O2} from sulfur content), although MiMIC (Rasmussen et al., 2020) can do calculations along constant volume paths and Petrolog4 has T as a dependent variable.
- Model-dependent variables: A wide variety of parameterisations for model-dependent variables are employed across the range of tools, especially in their chosen functional forms and parameterizations of the solubility functions employed.

Overall, VolFe is most similar to Evo, MAGEC, and the Gaillard tool in terms of the species and reactions considered in the melt and vapor but different parameterisations of model-dependent variables are available in the different tools.

7 Future work

Our goal is to make VolFe a flexible and adaptable tool for predicting and understanding trends relating to melt-vapor equilibrium in natural magmas based on a thermodynamically consistent framework. However, the data underlying VolFe is a moving target. As we have tried to emphasize, an important feature is the ability to update VolFe by modifying, and adding new options, to the existing parameterizations for model-dependent variables. Additionally, new calculation types can be

incorporated as they become useful. Features and/or data that we believe could enhance the utility of VolFe include, but are not limited to:

- Continued improvement of interoperability with other relevant Python packages: e.g., currently with PySulfSat (Wieser and Gleeson, 2023) and DensityX (Iacovino and Till, 2018), and in the future with packages such as Thermobar (Wieser et al., 2022b) and MELTS (Gualda et al., 2012).
- Expand the isobar calculations to include f_{O2} (or Fe^{3+}/Fe_T or S^{6+}/S_T) and sulfur, e.g., CO_2-eq and H_2O-eq at constant S_T and f_{O2}; S_T and H_2O-eq at constant CO_2-eq and Fe^{3+}/Fe_T; CO_2-eq and f_{O2} at constant H_2O-eq and S_T; etc.
- Calculation of vapor composition when vapor is the only phase present (e.g., Moussallam et al., 2022).
- Model the vapor as a real mixture of non-ideal species, which means the fugacity coefficients can depend on the vapor composition (e.g., Duan and Zhang, 2006).
- Include OH^- and H_2O_{mol} as melt species with ideal and regular solution models (e.g., Dixon et al., 1995; Lesne et al., 2011b; Newman and Lowenstern, 2002; Silver and Stolper, 1989) to more accurately model at higher water concentrations than is reasonable given the current Sievert's law approximation.
- An accurate, melt-composition-, *T*-, and *P*-dependent solubility constant for $CO_{2,T}$ that includes interactions between dissolved molecular CO_2 and dissolved carbonate species. The uncertainties and inconsistencies of available experimental data and models based on these data are a significant barrier to quantitative modelling of natural melt-vapor equilibria over the full range of magma compositions (e.g., Wieser et al., 2022a).
- Add parameterisations of solubility constants for other volatile species (e.g., noble gases: Iacono-Marziano et al., 2010; Lux, 1987)
- Cl as a component, Cl as a melt species, Cl_2 and HCl and vapor species, and brine as a saturating phase (e.g., Thomas and Wood, 2022).
- Evaluate and incorporate uncertainties on model-dependent variables into the calculations.
- Include crystallisation during ascent through coupling with programs like MELTS (Gualda et al., 2012) (e.g., MAGEC; Sun and Lee, 2022)
- Develop a function to calculate equilibrium with volume and *T* as the independent variables. This would be of value for modelling formation of "shrinkage bubbles" in melt inclusions during cooling (Zhang, 1998, e.g., MiMIC; Rasmussen et al., 2020) or rigid magma chamber cooling.
- Add calculations of equilibrium isotopic fractionation of stable isotopes between melt and vapor (e.g., Walter and Castro, 2020). This would provide a framework for quantitative interpretations of systematic variations of isotopic ratios observed in natural magmas (e.g., Aubaud et al., 2004; Newman et al., 1988; Taracsák et al., 2023).

- Finding the stable equilibrium state for the system that would include liquid sulfide and anhydrite phases by incremental "precipitation" of these phases followed by recalculation of the equilibrium state (considering that this will change the composition of the bulk silicate component) until the calculated equilibrium liquid is just saturated with one or more of these phases.
- Comparison and benchmarking with other melt-vapor chemical equilibria tools (e.g., Hughes et al., 2023).

8 Conclusions

We have outlined the thermodynamic framework and calculation types for VolFe, an open-source Python package to calculate melt-vapor equilibria. VolFe considers a variety of both oxidised and reduced volatile-bearing species containing C, H, S, O, and noble gases such that it can be applied to terrestrial (e.g., MORB, arc, and ocean islands) and extra-terrestrial (e.g., Moon, Mars, and Io) systems. Various parameterisations of model dependent variables (e.g., fugacity coefficients, equilibrium constants for homogeneous vapor equilibria, solubility functions for heterogeneous melt-vapor equilibria, saturation conditions, etc.) are available to enable modelling of basaltic through rhyolitic melts, with the hope that new parameterisations will be added as new studies are published. The main calculation types are the pressure of vapor-saturation and range in f_{O2} based on the measured sulfur content from melt inclusion and matrix glass data; as well as open- and closed-system re- and degassing paths. We applied VolFe calculations to data from the Marianas arc to illustrate the types of results that can be calculated from melt inclusion and matrix glass data.

9 Author contributions

ECH and EMS conceived the project. ECH is the main developer of VolFe with support from PL and PW and input on direction from EMS. ECH wrote the first draft of the manuscript and all authors contributed to subsequent drafts.

10 Acknowledgements

ECH was funded by a Caltech Geology Option Post-Doctoral Fellowship and a Caltech Centre for Comparative Planetary Evolution (^{3}CPE) research grant and is supported by the New Zealand Ministry of Business, Innovation and Employment (MBIE) through the Hazards and Risk Management (Strategic Science Investment Fund, contract C05X1702). PL acknowledges an

Embiricos Trust scholarship from Jesus College, University of Cambridge. PW acknowledges funding from a Sloan Research Fellowship.

11 Data availability

VolFe is freely available on github (https://github.com/eryhughes/VolFe), installable using PyPI (the version number should be stated for calculations used), and there is documentation on ReadTheDocs (https://volfe.readthedocs.io/en/latest/).

12 References

Aiuppa, A., Bitetto, M., Calabrese, S., Delle Donne, D., Lages, J., La Monica, F.P., Chiodini, G., Tamburello, G., Cotterill, A., Fulignati, P., Gioncada, A., Liu, E.J., Moretti, R., Pistolesi, M., 2022. Mafic magma feeds degassing unrest at Vulcano Island, Italy. Commun. Earth Environ. 2022 31 3, 1–15. https://doi.org/10.1038/s43247-022-00589-1

Allison, C.M., Roggensack, K., Clarke, A.B., 2022. MafiCH: a general model for H2O–CO2 solubility in mafic magmas. Contrib. to Mineral. Petrol. 177, 1–22. https://doi.org/10.1007/S00410-022-01903-Y/FIGURES/10

Allison, C.M., Roggensack, K., Clarke, A.B., 2019. H2O–CO2 solubility in alkali-rich mafic magmas: new experiments at mid-crustal pressures. Contrib. to Mineral. Petrol. 174, 58. https://doi.org/10.1007/s00410-019-1592-4

Anderson, A.T.J., Newman, S., Williams, S.N., Druitt, T.H., Skirius, C., Stolper, E.M., 1989. H2O, CO2, CI, and gas in Plinian and ash-flow Bishop rhyolite. Geology 17, 221–225. https://doi.org/10.1130/0091-7613(1989)017

Anderson, A.T.J., Wright, T.L., 1972. Phenocrysts and glass inclusions and their bearing on oxidation and mixing of basaltic magmas, kilauea volcano, hawaii. Am. Mineral. 57, 188–216.

Applegarth, L.J., Tuffen, H., James, M.R., Pinkerton, H., 2013. Degassing-driven crystallisation in basalts. Earth-Science Rev. 116, 1–16. https://doi.org/10.1016/J.EARSCIREV.2012.10.007

Ardia, P., Hirschmann, M.M., Withers, A.C., Stanley, B.D., 2013. Solubility of CH4 in a synthetic basaltic melt, with applications to atmosphere–magma ocean–core partitioning of volatiles and to the evolution of the Martian atmosphere. Geochim. Cosmochim. Acta 114, 52–71. https://doi.org/10.1016/J.GCA.2013.03.028

Armstrong, L.S., Hirschmann, M.M., Stanley, B.D., Falksen, E.G., Jacobsen, S.D., 2015. Speciation and solubility of reduced C-O-H-N volatiles in mafic melt: Implications for volcanism, atmospheric evolution, and deep volatile cycles in the terrestrial planets. Geochim. Cosmochim. Acta 171, 283–302. https://doi.org/10.1016/j.gca.2015.07.007

1083 Aubaud, C., Pineau, F., Jambon, A., Javoy, M., 2004. Kinetic disequilibrium of C, He, Ar and carbon
1084 isotopes during degassing of mid-ocean ridge basalts. Earth Planet. Sci. Lett. 222, 391–406.
1085 https://doi.org/10.1016/j.epsl.2004.03.001
1086 Baker, D.R., Moretti, R., 2011. Modeling the Solubility of Sulfur in Magmas: A 50-Year Old
1087 Geochemical Challenge. Rev. Mineral. Geochemistry 73, 167–213.
1088 https://doi.org/10.2138/RMG.2011.73.7
1089 Baumgartner, R.J., Baratoux, D., Gaillard, F., Fiorentini, M.L., 2017. Numerical modelling of erosion
1090 and assimilation of sulfur-rich substrate by martian lava flows: Implications for the genesis of
1091 massive sulfide mineralization on Mars. Icarus 296, 257–274.
1092 https://doi.org/10.1016/j.icarus.2017.06.016
1093 Beermann, O., Botcharnikov, R.E., Holtz, F., Diedrich, O., Nowak, M., 2011. Temperature
1094 dependence of sulfide and sulfate solubility in olivine-saturated basaltic magmas. Geochim.
1095 Cosmochim. Acta 75, 7612–7631. https://doi.org/10.1016/j.gca.2011.09.024
1096 Behrens, H., Ohlhorst, S., Holtz, F., Champenois, M., 2004. CO2 solubility in dacitic melts
1097 equilibrated with H2O-CO2 fluids: Implications for modeling the solubility of CO2 in silicic
1098 melts. Geochim. Cosmochim. Acta 68, 4687–4703. https://doi.org/10.1016/J.GCA.2004.04.019
1099 Belgrano, T.M., Tollan, P.M., Marxer, F., Diamond, L.W., 2021. Paleobathymetry of Submarine
1100 Lavas in the Samail and Troodos Ophiolites: Insights From Volatiles in Glasses and
1101 Implications for Hydrothermal Systems. J. Geophys. Res. Solid Earth 126, e2021JB021966.
1102 https://doi.org/10.1029/2021JB021966
1103 Belonoshko, A.B., Saxena, S.K., 1992. A unified equation of state for fluids of C-H-O-N-S-Ar
1104 composition and their mixtures up to very high temperatures and pressures. Geochim.
1105 Cosmochim. Acta 56, 3611–3626. https://doi.org/10.1016/0016-7037(92)90157-E
1106 Black, B.A., Andrews, B.J., 2020. Petrologic imaging of the architecture of magma reservoirs feeding
1107 caldera-forming eruptions. Earth Planet. Sci. Lett. 552, 116572.
1108 https://doi.org/10.1016/J.EPSL.2020.116572
1109 Blank, J.G., Brooker, R.A., 1994. Experimental studies of carbon dioxide in silicate melts: Solubility,
1110 speciation, and stable carbon isotope behaviour. Rev. Mineral. Geochemistry 30, 157–186.
1111 Blank, J.G., Stolper, E.M., Carroll, M.R., 1993. Solubilities of carbon dioxide and water in rhyolitic
1112 melt at 850°C and 750 bars. Earth Planet. Sci. Lett. 119, 27–36. https://doi.org/10.1016/0012-
1113 821X(93)90004-S
1114 Blundy, J.D., Cashman, K.V., 2008. Petrologic reconstruction of magmatic system variables and
1115 processes. Rev. Mineral. Geochemistry 69, 179–239.
1116 Borisov, A., Behrens, H., Holtz, F., 2018. Ferric/ferrous ratio in silicate melts: a new model for 1 atm
1117 data with special emphasis on the effects of melt composition. Contrib. to Mineral. Petrol. 173,
1118 1–15. https://doi.org/10.1007/S00410-018-1524-8/FIGURES/10
1119 Botcharnikov, R.E., Behrens, H., Holtz, F., 2006. Solubility and speciation of C–O–H fluids in

andesitic melt at T = 1100–1300 °C and P = 200 and 500 MPa. Chem. Geol. 229, 125–143. https://doi.org/10.1016/J.CHEMGEO.2006.01.016

Boulliung, J., Wood, B.J., 2023a. Sulfur oxidation state and solubility in silicate melts. Contrib. to Mineral. Petrol. 178, 1–15. https://doi.org/10.1007/S00410-023-02033-9/FIGURES/9

Boulliung, J., Wood, B.J., 2023b. Corrigendum to "SO2 solubility and degassing behavior in silicate melts" [Geochim. Cosmochim. Acta 336 (2022) 150–164]. Geochim. Cosmochim. Acta 343, 420. https://doi.org/10.1016/J.GCA.2022.11.025

Boulliung, J., Wood, B.J., 2022. SO2 solubility and degassing behavior in silicate melts. Geochim. Cosmochim. Acta Vol. , 1 Novemb. 2022, Pages 150-164 336, 150–164. https://doi.org/10.1016/j.gca.2022.08.032

Brooker, R.A., Kohn, S.C., Holloway, J.R., McMillan, P.F., Carroll, M.R., 1999. Solubility, speciation and dissolution mechanisms for CO2 in melts on the NaAlO2-SiO2 join. Geochim. Cosmochim. Acta 63, 3549–3565.

Brounce, M.N., Kelley, K.A., Cottrell, E., 2014. Variations in Fe3+/∑Fe of Mariana Arc Basalts and Mantle Wedge fO2. J. Petrol. 55, 2513–2536. https://doi.org/10.1093/PETROLOGY/EGU065

Brounce, M.N., Kelley, K.A., Stern, R., Martinez, F., Cottrell, E., 2016. The Fina Nagu volcanic complex: Unusual submarine arc volcanism in the rapidly deforming southern Mariana margin. Geochemistry, Geophys. Geosystems 17, 4078–4091. https://doi.org/10.1002/2016GC006457

Brounce, M.N., Stolper, E.M., Eiler, J.M., 2017. Redox variations in Mauna Kea lavas, the oxygen fugacity of the Hawaiian plume, and the role of volcanic gases in Earth's oxygenation. Proc. Natl. Acad. Sci. U. S. A. 114. https://doi.org/10.1073/pnas.1619527114

Burgisser, A., Alletti, M., Scaillet, B., 2015. Simulating the behavior of volatiles belonging to the C–O–H–S system in silicate melts under magmatic conditions with the software D-Compress. Comput. Geosci. 79, 1–14. https://doi.org/10.1016/J.CAGEO.2015.03.002

Burgisser, A., Scaillet, B., 2007. Redox evolution of a degassing magma rising to the surface. Nature 445, 194–197. https://doi.org/10.1038/nature05509

Burnham, C.W., 1979. The importance of volatile constituents, in: Yoder Jr, H.S. (Ed.), The Evolution of the Igneous Rocks: Fiftieth Anniversary Perspectives. University Press, Princeton, Princeton, pp. 439–482.

Burnham, C.W., Davis, N.F., 1974. The role of H 2 O in silicate melts; II, Thermodynamic and phase relations in the system NaAlSi 3 O 8 -H 2 O to 10 kilobars, 700 degrees to 1100 degrees C. Am. J. Sci. 274, 902–940. https://doi.org/10.2475/AJS.274.8.902

Burton, M., Aiuppa, A., Allard, P., Asensio-Ramos, M., Cofrades, A.P., La Spina, A., Nicholson, E.J., Zanon, V., Barrancos, J., Bitetto, M., Hartley, M., Romero, J.E., Waters, E., Stewart, A., Hernández, P.A., Lages, J.P., Padrón, E., Wood, K., Esse, B., Hayer, C., Cyrzan, K., Rose-Koga, E.F., Schiavi, F., D'Auria, L., Pérez, N.M., 2023. Exceptional eruptive CO2 emissions from intra-plate alkaline magmatism in the Canary volcanic archipelago. Commun. Earth Environ.

2023 41 4, 1–10. https://doi.org/10.1038/s43247-023-01103-x
Camejo-Harry, M., Melekhova, E., Blundy, J., Attridge, W., Robertson, R., Christopher, T., 2018. Magma evolution beneath Bequia, Lesser Antilles, deduced from petrology of lavas and plutonic xenoliths. Contrib. to Mineral. Petrol. 173, 1–26. https://doi.org/10.1007/S00410-018-1504-Z/FIGURES/14
Camejo-Harry, M., Melekhova, E., Blundy, J., Robertson, R., 2019. Evolution in magma storage conditions beneath Kick-'em-Jenny and Kick-'em-Jack submarine volcanoes, Lesser Antilles arc. J. Volcanol. Geotherm. Res. 373, 1–22. https://doi.org/10.1016/J.JVOLGEORES.2019.01.023
Candela, P.A., 1986. The evolution of aqueous vapor from silicate melts: Effect on oxygen fugacity. Geochim. Cosmochim. Acta 50, 1205–1211. https://doi.org/10.1016/0016-7037(86)90403-5
Carey, R.J., Manga, M., Degruyter, W., Gonnermann, H., Swanson, D., Houghton, B., Orr, T., Patrick, M., 2013. Convection in a volcanic conduit recorded by bubbles. Geology 41, 395–398. https://doi.org/10.1130/G33685.1
Carmichael, I.S.E., Ghiorso, M.S., 1990. The effect of oxygen fugacity on the redox state of natural liquids and their crystallizing phases. Rev. Mineral. Geochemistry 24, 191–212.
Carmichael, I.S.E., Ghiorso, M.S., 1986. Oxidation-reduction relations in basic magma: a case for homogeneous equilibria. Earth Planet. Sci. Lett. 78, 200–210. https://doi.org/10.1016/0012-821X(86)90061-0
Chowdhury, P., Dasgupta, R., 2019. Effect of sulfate on the basaltic liquidus and Sulfur Concentration at Anhydrite Saturation (SCAS) of hydrous basalts – Implications for sulfur cycle in subduction zones. Chem. Geol. 522, 162–174. https://doi.org/10.1016/J.CHEMGEO.2019.05.020
Clemente, B., SCAILLET, B., PICHAVANT, M., 2004. The Solubility of Sulphur in Hydrous Rhyolitic Melts. J. Petrol. 45, 2171–2196. https://doi.org/10.1093/petrology/egh052
Colman, A., Sinton, J.M., Wanless, V.D., 2015. Constraints from melt inclusions on depths of magma residence at intermediate magma supply along the Galápagos Spreading Center. Earth Planet. Sci. Lett. 412, 122–131. https://doi.org/10.1016/J.EPSL.2014.12.007
Coombs, M.L., Sisson, T.W., Lipman, P.W., 2006. Growth history of Kilauea inferred from volatile concentrations in submarine-collected basalts. J. Volcanol. Geotherm. Res. 151, 19–49. https://doi.org/10.1016/J.JVOLGEORES.2005.07.037
Ding, S., Plank, T., Wallace, P.J., Rasmussen, D.J., 2023. Sulfur_X: A Model of Sulfur Degassing During Magma Ascent. Geochemistry, Geophys. Geosystems 24, e2022GC010552. https://doi.org/10.1029/2022GC010552
Dingwell, D.B., Romano, C., Hess, K.U., 1996. The effect of water on the viscosity of a haplogranitic melt under P-T-X conditions relevant to silicic volcanism. Contrib. to Mineral. Petrol. 124, 19–28. https://doi.org/10.1007/S004100050170/METRICS
Dixon, J.E., 1997. Degassing of alkalic basalts. Am. Mineral. 82, 368–378.

https://doi.org/10.2138/AM-1997-3-415/MACHINEREADABLECITATION/RIS
Dixon, J.E., Stolper, E.M., 1995. An experimental study water and carbon dioxide solubilities in mid-ocean ridge basaltic liquids. Part II: Application to degassing. J. Petrol. 36, 1633–1646.
Dixon, J.E., Stolper, E.M., Holloway, J.R., 1995. An experimental study of water and carbon dioxide solubilities in mid-ocean ridge basaltic liquids. Part I: Calibration and solubility models. J. Petrol. 36, 1607–1631. https://doi.org/10.1093/oxfordjournals.petrology.a037267
Duan, Z., Zhang, Z., 2006. Equation of state of the H2O, CO2, and H2O–CO2 systems up to 10 GPa and 2573.15 K: Molecular dynamics simulations with ab initio potential surface. Geochim. Cosmochim. Acta 70, 2311–2324. https://doi.org/10.1016/J.GCA.2006.02.009
Fincham, C.J.B., Richardson, F.D., 1954. The behaviour of sulphur in silicate and aluminate melts. Proc. R. Soc. London. Ser. A. Math. Phys. Sci. 223, 40–62. https://doi.org/10.1098/rspa.1954.0099
Fine, G., Stolper, E., 1986. Dissolved carbon dioxide in basaltic glasses: concentrations and speciation. Earth Planet. Sci. Lett. 76, 263–278. https://doi.org/10.1016/0012-821X(86)90078-6
Fine, G., Stolper, E., 1985. The speciation of carbon dioxide in sodium aluminosilicate glasses. Contrib. to Mineral. Petrol. 91, 105–121. https://doi.org/10.1007/BF00377759/METRICS
Fortin, M.A., Riddle, J., Desjardins-Langlais, Y., Baker, D.R., 2015. The effect of water on the sulfur concentration at sulfide saturation (SCSS) in natural melts. Geochim. Cosmochim. Acta 160, 100–116. https://doi.org/10.1016/J.GCA.2015.03.022
Frost, B.R., 1991. Introduction to oxygen fugacity and its petrologic importance. Rev. Mineral. Geochemistry 25, 1–9.
Gaillard, F., Michalski, J., Berger, G., McLennan, S.M., Scaillet, B., 2013. Geochemical reservoirs and timing of sulfur cycling on Mars. Space Sci. Rev. https://doi.org/10.1007/s11214-012-9947-4
Gaillard, F., Scaillet, B., 2014. A theoretical framework for volcanic degassing chemistry in a comparative planetology perspective and implications for planetary atmospheres. Earth Planet. Sci. Lett. 403, 307–316. https://doi.org/10.1016/j.epsl.2014.07.009
Gaillard, F., Scaillet, B., 2009. The sulfur content of volcanic gases on Mars. Earth Planet. Sci. Lett. 279, 34–43. https://doi.org/10.1016/J.EPSL.2008.12.028
Gaillard, F., Scaillet, B., Arndt, N.T., 2011. Atmospheric oxygenation caused by a change in volcanic degassing pressure. Nature 478, 229–232. https://doi.org/10.1038/nature10460
Gaillard, F., Scaillet, B., Pichavant, M., Iacono-Marziano, G., 2015. The redox geodynamics linking basalts and their mantle sources through space and time. Chem. Geol. 418, 217–233. https://doi.org/10.1016/j.chemgeo.2015.07.030
Gaillard, F., Schmidt, B., Mackwell, S., McCammon, C., 2003. Rate of hydrogen–iron redox exchange in silicate melts and glasses. Geochim. Cosmochim. Acta 67, 2427–2441. https://doi.org/10.1016/s0016-7037(02)01407-2

Ghiorso, M.S., Gualda, G.A.R., 2015. An H2O–CO2 mixed fluid saturation model compatible with rhyolite-MELTS. Contrib. to Mineral. Petrol. 169, 53. https://doi.org/10.1007/s00410-015-1141-8

Ghiorso, M.S., Matthews, S., Sverjensky, D.A., 2023. MELTS+DEW: Modeling major element+Cl+F+S phase equilibria, redox reactions and elemental partitioning in magmatic-hydrothermal systems, in: Goldschmidt.

Gibbs, J.W., 1978. On the Equilibrium of Heterogeneous Substances. Trans. Connect. Acad. Arts Sci. 3, 343–524.

Gibbs, J.W., 1976. On the Equilibrium of Heterogeneous Substances. Trans. Connect. Acad. Arts Sci. 3, 108–248.

Gualda, G.A.R., Ghiorso, M.S., Lemons, R. V., Carley, T.L., 2012. Rhyolite-MELTS: a Modified Calibration of MELTS Optimized for Silica-rich, Fluid-bearing Magmatic Systems. J. Petrol. 53, 875–890. https://doi.org/10.1093/PETROLOGY/EGR080

Hirschmann, M.M., Withers, A.C., Ardia, P., Foley, N.T., 2012. Solubility of molecular hydrogen in silicate melts and consequences for volatile evolution of terrestrial planets. Earth Planet. Sci. Lett. 345–348, 38–48. https://doi.org/10.1016/J.EPSL.2012.06.031

Holland, T., Powell, R., 1991. A Compensated-Redlich-Kwong (CORK) equation for volumes and fugacities of CO2 and H2O in the range 1 bar to 50 kbar and 100–1600°C. Contrib. to Mineral. Petrol. 1991 1092 109, 265–273. https://doi.org/10.1007/BF00306484

Holloway, J.R., 1977. Fugacity and Activity of Molecular Species in Supercritical Fluids, in: Thermodynamics in Geology. Springer Netherlands, Dordrecht, pp. 161–181. https://doi.org/10.1007/978-94-010-1252-2_9

Holloway, J.R., Blank, J.G., 1994. Application of experimental results to C-O-H species in natural melts. Rev. Mineral. Geochemistry1 30, 187–230.

Holloway, J.R., Pan, V., Gudmundsson, G.B., 1992. High-pressure fluid-absent melting experiments in the presence of graphite: oxygen fugacity, ferric/ferrous ratio and dissolved CO2. Eur. J. Mineral. 4, 105–114.

Hughes, E.C., Ding, S., Iacovino, K., Wieser, P.E., Kilgour, G., 2023. Workshop report: Modelling volatile behaviour in magmas. Earth ArXiv. https://doi.org/10.31223/X5FD3Q

Hughes, E.C., Liggins, P., Saper, L., Stolper, E.M., 2024. The effects of oxygen fugacity and sulfur on the pressure of vapor-saturation of magma. Am. Mineral. 109, 422–438.

Hughes, E.C., Saper, L.M., Liggins, P., O'Neill, H.S.C., Stolper, E.M., 2022. The sulfur solubility minimum and maximum in silicate melt. J. Geol. Soc. London. 180, jgs2021-125. https://doi.org/https://doi.org/10.1144/jgs2021-125

Iacono-Marziano, G., Morizet, Y., Le Trong, E., Gaillard, F., 2012a. New experimental data and semi-empirical parameterization of H2O–CO2 solubility in mafic melts. Geochim. Cosmochim. Acta 97, 1–23. https://doi.org/10.1016/J.GCA.2012.08.035

Iacono-Marziano, G., Morizet, Y., Le Trong, E., Gaillard, F., 2012b. New experimental data and semi-empirical parameterization of H2O–CO2 solubility in mafic melts. Geochim. Cosmochim. Acta 97, 1–23. https://doi.org/10.1016/J.GCA.2012.08.035

Iacono-Marziano, G., Paonita, A., Rizzo, A., Scaillet, B., Gaillard, F., 2010. Noble gas solubilities in silicate melts: New experimental results and a comprehensive model of the effects of liquid composition, temperature and pressure. Chem. Geol. 279, 145–157. https://doi.org/10.1016/J.CHEMGEO.2010.10.017

Iacovino, K., Matthews, S., Wieser, P.E., Moore, G.M., Bégué, F., 2021. VESIcal Part I: An open-source thermodynamic model engine for mixed volatile (O-) solubility in silicate melts. Earth Sp. Sci. e2020EA001584. https://doi.org/10.1029/2020EA001584

Iacovino, K., Till, C., 2018. DensityX: A program for calculating the densities of hydrous magmatic liquids from 427-1,627 °C and up to 30 kbar. Volcanica 2, 1–10. https://doi.org/10.30909/vol.02.01.0110

Jugo, P.J., Wilke, M., Botcharnikov, R.E., 2010. Sulfur K-edge XANES analysis of natural and synthetic basaltic glasses: Implications for S speciation and S content as function of oxygen fugacity. Geochim. Cosmochim. Acta 74, 5926–5938. https://doi.org/10.1016/J.GCA.2010.07.022

Kadik, A.A., Lukanin, O.A., Lebedev, Y.B., Korovushkina, E.Y., 1972. Solubility of H2O and CO2 in granite and basalt melts at high pressures. Geochem. Int. 9, 1041–1050.

Kadik, A.A., Pineau, F., Litvin, Y., Jendrzejewski, N., Martinez, I., Javoy, M., 2004. Formation of Carbon and Hydrogen Species in Magmas at Low Oxygen Fugacity. J. Petrol. 45, 1297–1310. https://doi.org/10.1093/PETROLOGY/EGH007

Kelley, K.A., Cottrell, E., 2012. The influence of magmatic differentiation on the oxidation state of Fe in a basaltic arc magma. Earth Planet. Sci. Lett. 329–330, 109–121. https://doi.org/10.1016/j.epsl.2012.02.010

Kern, C., Aiuppa, A., de Moor, J.M., 2022. A golden era for volcanic gas geochemistry? Bull. Volcanol. 2022 845 84, 1–11. https://doi.org/10.1007/S00445-022-01556-6

King, P.L., Holloway, J.R., 2002. CO2 solubility and speciation in intermediate (andesitic) melts: the role of H2O and composition. Geochim. Cosmochim. Acta 66, 1627–1640. https://doi.org/10.1016/S0016-7037(01)00872-9

Klimm, K., Kohn, S.C., Botcharnikov, R.E., 2012a. The dissolution mechanism of sulphur in hydrous silicate melts. II: Solubility and speciation of sulphur in hydrous silicate melts as a function of fO2. Chem. Geol. 322–323, 250–267. https://doi.org/10.1016/J.CHEMGEO.2012.04.028

Klimm, K., Kohn, S.C., O'Dell, L.A., Botcharnikov, R.E., Smith, M.E., 2012b. The dissolution mechanism of sulphur in hydrous silicate melts. I: Assessment of analytical techniques in determining the sulphur speciation in iron-free to iron-poor glasses. Chem. Geol. 322–323, 237–249. https://doi.org/10.1016/J.CHEMGEO.2012.04.027

1305 Kolzenburg, S., Di Genova, D., Giordano, D., Hess, K.U., Dingwell, D.B., 2018. The effect of oxygen
1306 fugacity on the rheological evolution of crystallizing basaltic melts. Earth Planet. Sci. Lett. 487,
1307 21–32. https://doi.org/10.1016/J.EPSL.2018.01.023
1308 Kress, V.C., Carmichael, I.S.E., 1991. The compressibility of silicate liquids containing Fe2O3 and
1309 the effect of composition, temperature, oxygen fugacity and pressure on their redox states.
1310 Contrib. to Mineral. Petrol. 108, 82–92. https://doi.org/10.1007/BF00307328
1311 Lesne, P., Scaillet, B., Pichavant, M., 2015. The solubility of sulfur in hydrous basaltic melts. Chem.
1312 Geol. 418, 104–116. https://doi.org/10.1016/J.CHEMGEO.2015.03.025
1313 Lesne, P., Scaillet, B., Pichavant, M., Brey, G.P., 2011a. The carbon dioxide solubility in alkali
1314 basalts: an experimental study. Contrib. to Mineral. Petrol. 162, 153–168.
1315 https://doi.org/10.1007/s00410-010-0585-0
1316 Lesne, P., Scaillet, B., Pichavant, M., Iacono-Marziano, G., Beny, J.M., 2011b. The H2O solubility of
1317 alkali basaltic melts: An experimental study. Contrib. to Mineral. Petrol. 162, 133–151.
1318 https://doi.org/10.1007/S00410-010-0588-X/FIGURES/12
1319 Liggins, P., Jordan, S., Rimmer, P.B., Shorttle, O., 2022. Growth and Evolution of Secondary
1320 Volcanic Atmospheres: I. Identifying the Geological Character of Hot Rocky Planets. J.
1321 Geophys. Res. Planets 127, e2021JE007123. https://doi.org/10.1029/2021JE007123
1322 Liggins, P., Shorttle, O., Rimmer, P.B., 2020. Can volcanism build hydrogen-rich early atmospheres?
1323 Earth Planet. Sci. Lett. 550, 116546. https://doi.org/10.1016/J.EPSL.2020.116546
1324 Liu, K., Zhang, L., Guo, X., Ni, H., 2021. Effects of sulfide composition and melt H2O on sulfur
1325 content at sulfide saturation in basaltic melts. Chem. Geol. 559, 119913.
1326 https://doi.org/10.1016/j.chemgeo.2020.119913
1327 Liu, Y., Samaha, N.T., Baker, D.R., 2007. Sulfur concentration at sulfide saturation (SCSS) in
1328 magmatic silicate melts. Geochim. Cosmochim. Acta 71, 1783–1799.
1329 https://doi.org/10.1016/J.GCA.2007.01.004
1330 Lund, D.C., Seeley, E.I., Asimow, P.D., Lewis, M.J., McCart, S.E., Mudahy, A.A., 2018. Anomalous
1331 Pacific-Antarctic Ridge Volcanism Precedes Glacial Termination 2. Geochemistry, Geophys.
1332 Geosystems 19, 2478–2491. https://doi.org/10.1029/2017GC007341
1333 Lux, G., 1987. The behavior of noble gases in silicate liquids: Solution, diffusion, bubbles and surface
1334 effects, with applications to natural samples. Geochim. Cosmochim. Acta 51, 1549–1560.
1335 https://doi.org/10.1016/0016-7037(87)90336-X
1336 Macpherson, C.G., Mattey, D.P., 1994. Carbon isotope variations of CO2 in Central Lau Basin basalts
1337 and ferrobasalts. Earth Planet. Sci. Lett. 121, 263–276. https://doi.org/10.1016/0012-
1338 821X(94)90072-8
1339 Marshall, L.R., Maters, E.C., Schmidt, A., Timmreck, C., Robock, A., Toohey, M., 2022. Volcanic
1340 effects on climate: recent advances and future avenues. Bull. Volcanol. 2022 845 84, 1–14.
1341 https://doi.org/10.1007/S00445-022-01559-3

Matthews, S.J., Moncrieff, D.H.S., Carroll, M.R., 1999. Empirical Calibration of the Sulphur Valence Oxygen Barometer from Natural and Experimental Glasses: Method and Applications. Mineral. Mag. 63, 421–431. https://doi.org/10.1180/002646199548510

Métrich, N., Berry, A.J., O'Neill, H.S.C., Susini, J., 2009. The oxidation state of sulfur in synthetic and natural glasses determined by X-ray absorption spectroscopy. Geochim. Cosmochim. Acta 73, 2382–2399. https://doi.org/10.1016/J.GCA.2009.01.025

Meurer, A., Smith, C., Paprocki, M., Čertík, O., Kirpichev, S., Rocklin, M., Kumar, A., Ivanov, S., Moore, J., Singh, S., Rathnayake, T., Vig, S., Granger, B., Muller, R., Bonazzi, F., Gupta, H., Vats, S., Johansson, F., Pedregosa, F., Curry, M., Terrel, A., Roučka, Š., Saboo, A., Fernando, I., Kulal, S., Cimrman, R., A, S., 2017. SymPy: symbolic computing in Python. PeerJ Comput. Sci. 3, e103.

Moore, G., Vennemann, T., Carmichael, I.S.E., 1998. An empirical model for the solubility of H 2 O in magmas to 3 kilobars. Am. Mineral. 83, 36–42. https://doi.org/10.2138/AM-1998-1-203

Moore, J.G., Fornari, D.J., Clague, D.A., 1985. Basalts from the 1877 submarine eruption of Mauna Loa, Hawaii; new data on the variation of palagonitization rate with temperature, Bulletin. https://doi.org/10.3133/b1663

Moore, L.R., Bodnar, R.J., 2019. A pedagogical approach to estimating the co2 budget of magmas. J. Geol. Soc. London. 176, 398–407. https://doi.org/10.1144/JGS2018-094/ASSET/FC74300B-06F9-4FA7-85E5-C05E16121F7D/ASSETS/IMAGES/LARGE/JGS2018-094.05.JPG

Moretti, R., 2021. Ionic Syntax and Equilibrium Approach to Redox Exchanges in Melts: Basic Concepts and the Case of Iron and Sulfur in Degassing Magmas, in: Moretti, R., Neuville, D.R. (Eds.), Magma Redox Geochemistry, Geophysical Monograph Series. American Geophysical Union (AGU), pp. 115–138. https://doi.org/10.1002/9781119473206.CH6

Moretti, R., Ottonello, G., 2005. Solubility and speciation of sulfur in silicate melts: The Conjugated Toop-Samis-Flood-Grjotheim (CTSFG) model. Geochim. Cosmochim. Acta 69, 801–823. https://doi.org/10.1016/J.GCA.2004.09.006

Moretti, R., Ottonello, G., 2003. Polymerization and disproportionation of iron and sulfur in silicate melts: Insights from an optical basicity-based approach, in: Journal of Non-Crystalline Solids. North-Holland, pp. 111–119. https://doi.org/10.1016/S0022-3093(03)00297-7

Moretti, R., Papale, P., 2004. On the oxidation state and volatile behavior in multicomponent gas-melt equilibria. Chem. Geol. 213, 265–280. https://doi.org/10.1016/j.chemgeo.2004.08.048

Moretti, R., Papale, P., Ottonello, G., 2003. A model for the saturation of C-O-H-S fluids in silicate melts. Geol. Soc. London, Spec. Publ. 213, 81–101. https://doi.org/10.1144/GSL.SP.2003.213.01.06

Moune, S., Holtz, F., Botcharnikov, R.E., 2009. Sulphur solubility in andesitic to basaltic melts: implications for Hekla volcano. Contrib. to Mineral. Petrol. 157, 691–707. https://doi.org/10.1007/s00410-008-0359-0

1379 Moussallam, Y., Edmonds, M., Scaillet, B., Peters, N., Gennaro, M.E., Sides, I., Oppenheimer, C.,
1380 2016. The impact of degassing on the oxidation state of basaltic magmas: A case study of
1381 Kīlauea volcano. Earth Planet. Sci. Lett. 450, 317–325.
1382 https://doi.org/10.1016/j.epsl.2016.06.031
1383 Moussallam, Y., Oppenheimer, C., Scaillet, B., 2022. A novel approach to volcano surveillance using
1384 gas geochemistry. Comptes Rendus - Geosci. 355, 1–14.
1385 https://doi.org/10.5802/CRGEOS.158/FILE/ATTACH/CRGEOS-158-SUPPL.PDF
1386 Moussallam, Y., Oppenheimer, C., Scaillet, B., 2019. On the relationship between oxidation state and
1387 temperature of volcanic gas emissions. Earth Planet. Sci. Lett. 520, 260–267.
1388 https://doi.org/10.1016/J.EPSL.2019.05.036
1389 Moussallam, Y., Oppenheimer, C., Scaillet, B., Gaillard, F., Kyle, P., Peters, N., Hartley, M.E., Berlo,
1390 K., Donovan, A., 2014. Tracking the changing oxidation state of Erebus magmas, from mantle
1391 to surface, driven by magma ascent and degassing. Earth Planet. Sci. Lett. 393, 200–209.
1392 https://doi.org/10.1016/j.epsl.2014.02.055
1393 Muth, M.J., Wallace, P.J., 2022. Sulfur recycling in subduction zones and the oxygen fugacity of
1394 mafic arc magmas. Earth Planet. Sci. Lett. 599, 117836.
1395 https://doi.org/10.1016/J.EPSL.2022.117836
1396 Mysen, B., 2013. Structure–property relationships of COHN-saturated silicate melt coexisting with
1397 COHN fluid: A review of in-situ, high-temperature, high-pressure experiments. Chem. Geol.
1398 346, 113–124. https://doi.org/10.1016/J.CHEMGEO.2012.10.006
1399 Mysen, B.O., Kumamoto, K., Cody, G.D., Fogel, M.L., 2011. Solubility and solution mechanisms of
1400 C–O–H volatiles in silicate melt with variable redox conditions and melt composition at upper
1401 mantle temperatures and pressures. Geochim. Cosmochim. Acta 75, 6183–6199.
1402 https://doi.org/10.1016/J.GCA.2011.07.035
1403 Mysen, B.O., Virgo, D., Harrison, W.J., Scarfe, C.M., 1980. Solubility mechanisms of H2O in silicate
1404 melts at high pressures and temperatures: a Raman spectroscopic study | American Mineralogist
1405 | GeoScienceWorld. Am. Mineral. 65, 900–914.
1406 Newman, S., Epstein, S., Stolper, E.M., 1988. Water, carbon dioxide, and hydrogen isotopes in
1407 glasses from the ca. 1340 A.D. eruption of the Mono Craters, California: Constraints on
1408 degassing phenomena and initial volatile content. J. Volcanol. Geotherm. Res. 35, 75–96.
1409 https://doi.org/10.1016/0377-0273(88)90007-8
1410 Newman, S., Lowenstern, J.B., 2002. VolatileCalc: a silicate melt–H2O–CO2 solution model written
1411 in Visual Basic for excel. Comput. Geosci. 28, 597–604. https://doi.org/10.1016/S0098-
1412 3004(01)00081-4
1413 O'Neill, H.S.C., 2021. The thermodynamic controls on sulfide saturation in silicate melts with
1414 application to Ocean Floor Basalts., in: Moretti, R., Neuville, D.R. (Eds.), Magma Redox
1415 Geochemistry, Geophysical Monograph Series. John Wiley & Sons, Inc., pp. 177–213.

https://doi.org/10.1002/9781119473206.ch10
O'Neill, H.S.C., 1987. Quartz-fayalite-iron and quartz-fayalite-magnetite equilibria and the free energy of formation of fayalite (Fe2SiO4) and magnetite (Fe3O4). Am. Mineral. 72, 67–75.
O'Neill, H.S.C., Berry, A.J., Mallmann, G., 2018. The oxidation state of iron in Mid-Ocean Ridge Basaltic (MORB) glasses: Implications for their petrogenesis and oxygen fugacities. Earth Planet. Sci. Lett. 504, 152–162. https://doi.org/10.1016/J.EPSL.2018.10.002
O'Neill, H.S.C., Mavrogenes, J.A., 2022. The sulfate capacities of silicate melts. Geochim. Cosmochim. Acta. https://doi.org/10.1016/J.GCA.2022.06.020
O'Neill, H.S.C., Mavrogenes, J.A., 2002. The sulfide capacity and the sulfur content at sulfide saturation of silicate melts at 1400°C and 1 bar. J. Petrol. 43, 1049–1087. https://doi.org/10.1093/petrology/43.6.1049
Ohmoto, H., Kerrick, D.M., 1977. Devolatilization equilibria in graphitic systems. Am. J. Sci. 277, 1013–1044. https://doi.org/10.2475/AJS.277.8.1013
Papale, P., Moretti, R., Barbato, D., 2006. The compositional dependence of the saturation surface of H2O+CO2 fluids in silicate melts. Chem. Geol. 229, 78–95. https://doi.org/10.1016/j.chemgeo.2006.01.013
Papale, P., Moretti, R., Paonita, A., 2022. Thermodynamics of Multi-component Gas–Melt Equilibrium in Magmas: Theory, Models, and Applications. Rev. Mineral. Geochemistry 87, 431–556. https://doi.org/10.2138/RMG.2022.87.10
Paris, E., Giuli, G., Carroll, M.R., Davoli, I., 2001. The valence and speciation of sulfur in glasses by X-ray absorption spectroscopy. Can. Mineral. 39, 331–339. https://doi.org/10.2113/gscanmin.39.2.331
Prigogine, I., Defay, R., 1954. Treatise on Thermodynamics Based on the Methods of Gibbs and De Donder. Longmans, Green, London.
Putirka, K.D., 2008. Thermometers and Barometers for Volcanic Systems. Rev. Mineral. Geochemistry 69, 61–120. https://doi.org/10.2138/rmg.2008.69.3
Ranta, E., Halldórsson, S.A., Óladóttir, B.A., Pfeffer, M.A., Caracciolo, A., Bali, E., Guðfinnsson, G.H., Kahl, M., Barsotti, S., 2024. Magmatic Controls on Volcanic Sulfur Emissions at the Iceland Hotspot. Geochemistry, Geophys. Geosystems 25, e2024GC011443. https://doi.org/10.1029/2024GC011443
Rasmussen, D.J., Plank, T.A., Wallace, P.J., Newcombe, M.E., Lowenstern, J.B., 2020. Vapor-bubble growth in olivine-hosted melt inclusions. Am. Mineral. 105, 1898–1919. https://doi.org/10.2138/AM-2020-7377
Rose-Koga, E.F., Bouvier, A.S., Gaetani, G.A., Wallace, P.J., Allison, C.M., Andrys, J.A., Angeles de la Torre, C.A., Barth, A., Bodnar, R.J., Bracco Gartner, A.J.J., Butters, D., Castillejo, A., Chilson-Parks, B., Choudhary, B.R., Cluzel, N., Cole, M., Cottrell, E., Daly, A., Danyushevsky, L. V., DeVitre, C.L., Drignon, M.J., France, L., Gaborieau, M., Garcia, M.O., Gatti, E., Genske,

F.S., Hartley, M.E., Hughes, E.C., Iveson, A.A., Johnson, E.R., Jones, M., Kagoshima, T., Katzir, Y., Kawaguchi, M., Kawamoto, T., Kelley, K.A., Koornneef, J.M., Kurz, M.D., Laubier, M., Layne, G.D., Lerner, A.H., Lin, K.Y., Liu, P.P., Lorenzo-Merino, A., Luciani, N., Magalhães, N., Marschall, H.R., Michael, P.J., Monteleone, B.D., Moore, L.R., Moussallam, Y., Muth, M., Myers, M.L., Narváez, D.F., Navon, O., Newcombe, M.E., Nichols, A.R.L., Nielsen, R.L., Pamukcu, A., Plank, T., Rasmussen, D.J., Roberge, J., Schiavi, F., Schwartz, D., Shimizu, K., Shimizu, N., Thomas, J.B., Thompson, G.T., Tucker, J.M., Ustunisik, G., Waelkens, C., Zhang, Y., Zhou, T., 2021. Silicate melt inclusions in the new millennium: A review of recommended practices for preparation, analysis, and data presentation. Chem. Geol. 570, 120145. https://doi.org/10.1016/j.chemgeo.2021.120145

Sack, R.O., Carmichael, I.S.E., Rivers, M., Ghiorso, M.S., 1981. Ferric-ferrous equilibria in natural silicate liquids at 1 bar. Contrib. to Mineral. Petrol. 75, 369–376. https://doi.org/10.1007/BF00374720/METRICS

Seaman, C., Sherman, S.B., Garcia, M.O., Baker, M.B., Balta, B., Stolper, E.M., 2004. Volatiles in glasses from the HSDP2 drill core. Geochemistry, Geophys. Geosystems 5. https://doi.org/10.1029/2003GC000596

Shaw, H.R., Wones, D.R., 1964. Fugacity coefficients for hydrogen gas between 0 degrees and 1000 degrees C, for pressures to 3000 atm. Am. J. Sci. 262, 918–929. https://doi.org/10.2475/AJS.262.7.918

Shi, P., Saxena, S.K., 1992. Thermodynamic modeing of the C-H-O-S fluid system. Am. Mineral. 77, 1038–1049.

Shishkina, T.A., Botcharnikov, R.E., Holtz, F., Almeev, R.R., Jazwa, A.M., Jakubiak, A.A., 2014. Compositional and pressure effects on the solubility of H2O and CO2 in mafic melts. Chem. Geol. 388, 112–129. https://doi.org/10.1016/J.CHEMGEO.2014.09.001

Silver, L.A., Ihinger, P.D., Stolper, E.M., 1990. The influence of bulk composition on the speciation of water in silicate glasses. Contrib. to Mineral. Petrol. 104, 142–162. https://doi.org/10.1007/BF00306439

Silver, L.A., Stolper, E.M., 1989. Water in albitic glasses. J. Petrol. 30, 667–709. https://doi.org/10.1093/petrology/30.3.667

Simon, A.C., Ripley, E.M., 2011. The Role of Magmatic Sulfur in the Formation of Ore Deposits. Rev. Mineral. Geochemistry 73, 513–578. https://doi.org/10.2138/RMG.2011.73.16

Smythe, D.J., Wood, B.J., Kiseeva, E.S., 2017. The S content of silicate melts at sulfide saturation: New experiments and a model incorporating the effects of sulfide composition. Am. Mineral. 102, 795–803. https://doi.org/10.2138/AM-2017-5800CCBY

Soule, S.A., Nakata, D.S., Fornari, D.J., Fundis, A.T., Perfit, M.R., Kurz, M.D., 2012. CO2 variability in mid-ocean ridge basalts from syn-emplacement degassing: Constraints on eruption dynamics. Earth Planet. Sci. Lett. 327–328, 39–49. https://doi.org/10.1016/J.EPSL.2012.01.034

Spera, F.J., Bergman, S.C., 1980. Carbon Dioxide in igneous petrogenesis: I. Contrib. to Mineral. Petrol. 74, 55–66. https://doi.org/10.1007/BF00375489

Stanley, B.D., Hirschmann, M.M., Withers, A.C., 2014. Solubility of COH volatiles in graphite-saturated martian basalts. Geochim. Cosmochim. Acta 129, 54–76. https://doi.org/10.1016/j.gca.2013.12.013

Stewart, C., Damby, D.E., Horwell, C.J., Elias, T., Ilyinskaya, E., Tomašek, I., Longo, B.M., Schmidt, A., Carlsen, H.K., Mason, E., Baxter, P.J., Cronin, S., Witham, C., 2021. Volcanic air pollution and human health: recent advances and future directions. Bull. Volcanol. 2021 841 84, 1–25. https://doi.org/10.1007/S00445-021-01513-9

Stolper, E.M., 1982a. Water in silicate glasses: An infrared spectroscopic study. Contrib. to Mineral. Petrol. 81, 1–17. https://doi.org/10.1007/BF00371154

Stolper, E.M., 1982b. The speciation of water in silicate melts. Geochim. Cosmochim. Acta 46, 2609–2620.

Stolper, E.M., Fine, G., Johnson, T., Newman, S., 1987. Solubility of carbon dioxide in albitic melt. Am. Mineral. 72, 1071–1085.

Stolper, E.M., Holloway, J.R., 1988a. Experimental determination of the solubility of carbon dioxide in molten basalt at low pressure. Earth Planet. Sci. Lett. 87.

Stolper, E.M., Holloway, J.R., 1988b. Experimental determination of the solubility of carbon dioxide in molten basalt at low pressure. Earth Planet. Sci. Lett. 87, 397–408. https://doi.org/10.1016/0012-821X(88)90004-0

Sun, C., Lee, C.-T.A., 2022. Redox evolution of crystallizing magmas with C-H-O-S volatiles and its implications for atmospheric oxygenation. Geochim. Cosmochim. Acta 338, 302–321.

Sun, C., Yao, L., 2024. Redox equilibria of iron in low- to high-silica melts: A simple model and its applications to C-H-O-S degassing. Earth Planet. Sci. Lett. 638, 118742. https://doi.org/10.1016/J.EPSL.2024.118742

Taracsák, Z., Mather, T.A., Ding, S., Plank, T., Brounce, M., Pyle, D.M., Aiuppa, A., EIMF, 2023. Sulfur from the subducted slab dominates the sulfur budget of the mantle wedge under volcanic arcs. Earth Planet. Sci. Lett. 602, 117948. https://doi.org/10.1016/J.EPSL.2022.117948

Thibault, Y., Holloway, J.R., 1994. Solubility of CO2 in a Ca-rich leucitite: effects of pressure, temperature, and oxygen fugacity. Contrib. to Mineral. Petrol. 116, 216–224. https://doi.org/10.1007/BF00310701/METRICS

Thomas, R.W., Wood, B.J., 2022. The effect of composition on chlorine solubility and behaviour in silicate melts. Am. Mineral.

Wallace, P.J., Carmichael, I.S.E., 1994. S speciation in submarine basaltic glasses as determined by measurements of SKa X-ray wavelength shifts. Am. Mineral. 79, 161–167.

Walter, S.C., Castro, J.M., 2020. VolcDeGas: A program for modelling hydrogen isotope fractionation during degassing of rhyolitic melts. Volcanica 3, 155–168.

https://doi.org/10.30909/VOL.03.01.155168
Wanless, V.D., Shaw, A.M., Behn, M.D., Soule, S.A., Escartín, J., Hamelin, C., 2015. Magmatic plumbing at Lucky Strike volcano based on olivine-hosted melt inclusion compositions. Geochemistry, Geophys. Geosystems 16, 126–147. https://doi.org/10.1002/2014GC005517
Werner, C., Rasmussen, D.J., Plank, T., Kelly, P.J., Kern, C., Lopez, T., Gliss, J., Power, J.A., Roman, D.C., Izbekov, P., Lyons, J., 2020. Linking Subsurface to Surface Using Gas Emission and Melt Inclusion Data at Mount Cleveland Volcano, Alaska. Geochemistry, Geophys. Geosystems 21, e2019GC008882. https://doi.org/10.1029/2019GC008882
Wetzel, D.T., Rutherford, M.J., Jacobsen, S.D., Hauri, E.H., Saal, A.E., 2013. Degassing of reduced carbon from planetary basalts. Proc. Natl. Acad. Sci. 110, 8010–8013. https://doi.org/10.1073/PNAS.1219266110
Wieser, P.E., Gleeson, M., 2023. PySulfSat: An open-source Python3 tool for modeling sulfide and sulfate saturation. Volcanica 6, 107–127. https://doi.org/10.30909/VOL.06.01.107127
Wieser, P.E., Iacovino, K., Matthews, S., Moore, G., Allison, C.M., 2022a. VESIcal: 2. A Critical Approach to Volatile Solubility Modeling Using an Open-Source Python3 Engine. Earth Sp. Sci. 9, e2021EA001932. https://doi.org/10.1029/2021EA001932
Wieser, P.E., Lamadrid, H., Maclennan, J., Edmonds, M., Matthews, S., Iacovino, K., Jenner, F.E., Gansecki, C., Trusdell, F., Lee, R.L., Ilyinskaya, E., 2021. Reconstructing Magma Storage Depths for the 2018 Kīlauean Eruption From Melt Inclusion CO2 Contents: The Importance of Vapor Bubbles. Geochemistry, Geophys. Geosystems 22, e2020GC009364. https://doi.org/10.1029/2020GC009364
Wieser, P.E., Petrelli, M., Lubbers, J., Wieser, E., Özaydın, S., Kent, A.J.R., Till, C.B., 2022b. Thermobar: An open-source Python3 tool for thermobarometry and hygrometry. Volcanica 5, 349–384. https://doi.org/10.30909/VOL.05.02.349384
Wilke, M., Klimm, K., Kohn, S.C., 2011. Spectroscopic studies on sulfur speciation in synthetic and natural glasses. Rev. Mineral. Geochemistry 73, 41–78. https://doi.org/10.2138/rmg.2011.73.3
Witham, F., Blundy, J.D., Kohn, S.C., Lesne, P., Dixon, J.E., Churakov, S. V., Botcharnikov, R.E., 2012. SolEx: A model for mixed COHSCl-volatile solubilities and exsolved gas compositions in basalt. Comput. Geosci. 45, 87–97. https://doi.org/10.1016/j.cageo.2011.09.021
Yoshioka, T., Nakashima, D., Nakamura, T., Shcheka, S., Keppler, H., 2019. Carbon solubility in silicate melts in equilibrium with a CO-CO2 gas phase and graphite. Geochim. Cosmochim. Acta 259, 129–143. https://doi.org/10.1016/J.GCA.2019.06.007
Zajacz, Z., Tsay, A., 2019. An accurate model to predict sulfur concentration at anhydrite saturation in silicate melts. Geochim. Cosmochim. Acta 261, 288–304. https://doi.org/10.1016/J.GCA.2019.07.007
Zhang, Y., 1998. Mechanical and phase equilibria in inclusion–host systems. Earth Planet. Sci. Lett. 157, 209–222. https://doi.org/10.1016/S0012-821X(98)00036-3

Supplementary Material for Hughes et al.

"VolFe: an open-source tool for calculating melt-vapor equilibria including silicate melt, carbon, hydrogen, sulfur, and noble gases"

1 Parameterisations for model dependent variables

1.1 New parameterisations

The solubility constant for water in rhyolite was parameterised from the experimental data of Blank et al. (1993), Kadik et al. (1972), and Silver et al. (1990) in Figure 3 of Blank et al. (1993) as shown in Figure S10.

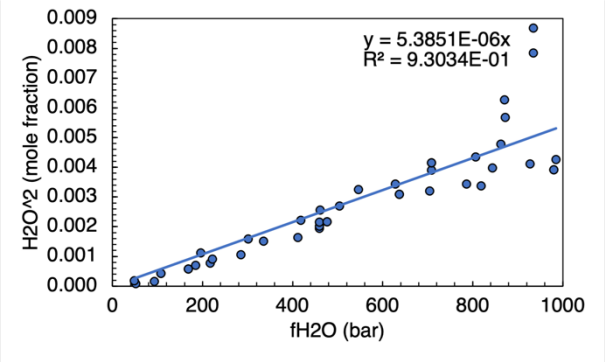

Figure S10. Water concentration against f_{H2O} for rhyolitic melts from the experimental data of Blank et al. (1993), Kadik et al. (1972), and Silver et al. (1990) in Figure 3 of Blank et al. (1993). The coefficient in the equation is the water solubility function for rhyolite.

The solubility constants for Ar and Ne in basalt and rhyolite were parameterised from the experimental data of Iacono-Marziano et al. (2010) as shown in Figure S11.

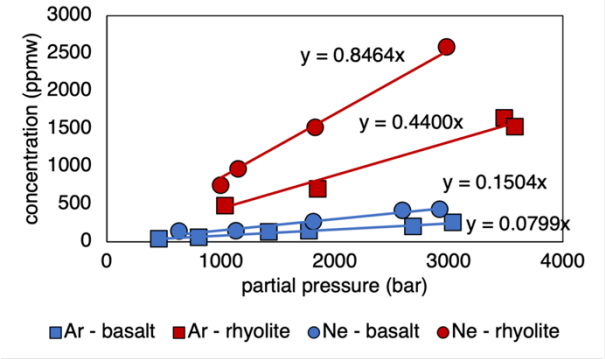

Figure S11. Concentration against partial pressure for Ar (squares) and Ne (circles) in basalt (blue) and rhyolite (red) using experimental data from Iacono-Marziano et al. (2010). The coefficient in each equation is the value of the solubility constant.

1.2 Currently available parameterisations in VolFe

Experimental conditions (P, T, and melt composition) of the data used to calibrate the various solubility constants are listed in Table S6 to Table S12 as an indication of the range of conditions they might be appropriate for.

Table S4. Equilibrium constants for homogeneous vapor equilibria in Table 1 of the main text.

Equilibrium constant	Reference
K_H	Reaction (d) in Table 1 of Ohmoto and Kerrick (1977)
K_C	Reaction (c) in Table 1 of Ohmoto and Kerrick (1977)
K_S	Reaction (f) in Table 1 of Ohmoto and Kerrick (1977)
K_{CH}	Reaction (e) in Table 1 of Ohmoto and Kerrick (1977)
K_{HS}	Reaction (h) in Table 1 of Ohmoto and Kerrick (1977)
K_{SC}	Eq. (8) in Moussallam et al. (2019)
K_{S2}^*	Eq (6b) in O'Neill and Mavrogenes (2022)

Note: $^*K_{S2} = f_{SO3}/f_{O2}^{1.5}f_{S2}^{0.5}$ – this is not a reaction in VolFe (i.e., SO_3 is not a vapor species present), but this is required to use the O'Neill and Mavrogenes (2022) sulfate capacity.

Table S5. Fugacity coefficients and their calibration ranges.

Species	P (bar)	T (°C)	Reference
All	1	n/a	Ideal
O_2	51–20000	-118–2227	Shi and Saxena (1992)
H_2	1–3040	0–1000	Shaw and Wones (1964)
S_2	73–20000	-65–2227	Shi and Saxena (1992)
CO	35–20000	-140–2227	Shi and Saxena (1992)
H_2O	1–50000	100–1400	Holland and Powell (1991)
CO_2	74–20000	31–2227	Shi and Saxena (1992)
	1–8000	200–1600	Holland and Powell (1991)
SO_2	78–20000	158–2227	Shi and Saxena (1992)
	78–20000	158–2227	Figure S1 from Hughes et al. (2022) based on Shi and Saxena (1992)
H_2S	90–20000	101–2227	Shi and Saxena (1992)
	90–20000	101–2227	Figure S1 from Hughes et al. (2024) based on Shi and Saxena (1992)
CH_4	46–20000	-82–2227	Shi and Saxena (1992)
OCS	66–20000	105–2227	Shi and Saxena (1992)

Table S6. Solubility constant for $CO_{2,T}$ and range of conditions of experiments used for calibration.

Variables	T (°C)	P (bars)	Composition	Reference
P	1170–1600	201–15000	MORB	Bullet (5) of summary from Dixon et al. (1995), which includes values from Pan et al. (1991)
P, X_{sil}	1170–1600	1000–15000	Basalt	Eq. (7) from Dixon (1997) as shown in eq. (1, 5) from Witham et al. (2012),

				which includes values from Pan et al. (1991)
P, SiO_2	1170–1600	1000–15000	Basalt (North Arch)	Eq. (8) from Dixon (1997), which includes values from Pan et al. (1991)
P, X_{sil}	1200	269–2059	Basalt	Eq. (25, 26) from Lesne et al. (2011a)
P	1200	269–2059	Alkali basalt (Vesuvius)	VES-9 in Table 4 from Lesne et al. (2011a)
P	1200	269–2059	Alkali basalt (Etna)	ETN-1 in Table 4 from Lesne et al. (2011a)
P	1200	269–2059	Alkali basalt (Stromboli)	PST-9 in Table 4 from Lesne et al. (2011a)
P	1200	4071–6098	Alkali basalt (Sunset Crater)	Sunset Crater in Table 4 from Allison et al. (2019)
P	1200	4133–6123	Basaltic andesite (SFVF)	SFVF in Table 4 from Allison et al. (2019)
P	1200	4078–6175	Phonotephrite (Erebus)	Erebus in Table 4 from Allison et al. (2019)
P	1200	269–6221	Phonotephrite (Vesuvius)	Vesuvius in Table 4 from Allison et al. (2019)
P	1200	485–6199	Trachybasalt (Etna)	Etna in Table 4 from Allison et al. (2019)
P	1200	524–6080	Alkali basalt (Stromboli)	Stromboli in Table 4 from Allison et al. (2019)
P, T	1200	10000–20000	Basanite	Basanite in Table 5 of Holloway and Blank,(1994)
P, T	1200–1600	1000–20000	Leucitite	Thibault and Holloway (1994)
P	1250	500–5000	Tholeiite basalt	N72 basalt in Table 2 from Allison et al. (2022), based on experiments of Shishkina et al. (2010)
P, T	750–1150	200–6600	Rhyolite	Fig. 2 caption from Blank et al. (1993), based on data from Blank (1993) and Fogel and Rutherford (1990)

Table S7. Equilibrium constant for $CO_{2,mol}$ and CO_3^{2-} and range of conditions of experiments used for calibration.

Variables	T (°C)	P (bars)	Composition	Reference
Constant	n/a	n/a	Basalt	Based on observation that all oxidised carbon is CO_3^{2-} in basalts (e.g., Fine and Stolper, 1986)
T	1100–1300	2000–5000	Andesite	Eq. (8) from Botcharnikov et al. (2006)
T	1250	1000–5000	Dacite	Eq. in the text from Botcharnikov et al. (2006), based on data from Behrens et al. (2004)
Constant	n/a	n/a	Rhyolite	Based on observation that all oxidised carbon is $CO_{2,T}$ in rhyolites (e.g., Blank et al., 1993a)

Table S8. Solubility constant for H_2O_T and range of conditions of experiments used for calibration.

Variables	T (°C)	P (bars)	Composition	Reference
Constant	1050–1250	109–5000	Basalt (< 6 wt% H_2O_T)	Figure S2 from Hughes et al. (2024b) based on data compilation from Allison et al. (2022)
Constant	850–1200	49–2000	Rhyolite	Figure S10, based on data from Blank et al. (1993), Kadik et al. (1972), and Silver et al. (1990)

Table S9. Solubility constants for sulfide and range of conditions of experiments used for calibration.

Variables	T (°C)	P (bars)	Composition	Reference
T, X_{sil}	1200–1500	1	Anhydrous basalt to rhyolite	Eq. (10.34) from O'Neill (2021) (with or without dilution from H_2O), based on data from Haughton et al. (1974), O'Neill and Mavrogenes (2002), and Tuff and O'Neill (2010)
T, X_{sil}	1045–1500	1–15000	Hydrous basalt to rhyolite	Eq. (10.34, 10.49) from O'Neill (2021)
T, X_{sil}	1000–1500	1	Anhydrous basalt to andesite	Eq. (6) from Boulliung and Wood (2023a)
T, X_{sil}	1000–1500	1	Anhydrous basalt to rhyolite	Eq. (7) from Boulliung and Wood (2023a)

Table S10. Solubility constants for sulfate and range of conditions of experiments used for calibration.

Variables	T (°C)	P (bars)	Composition	Reference
T, X_{sil}	1200–1500	1	Anhydrous basalt to rhyolite	Eq. (12a) from O'Neill and Mavrogenes (2022) (with or without dilution from H_2O)
T, X_{sil}	1200–1500	1	Anhydrous basalt to rhyolite	Eq. (5) from Boulliung and Wood (2023b)
P, T, X_{sil}	1200–1500	1	Anhydrous basalt to rhyolite	Eq. (5) from Boulliung and Wood (2023b) and eq. (8) from Boulliung and Wood (2022)
T, X_{sil}	1200–1500	1	Anhydrous basalt to rhyolite	Eq. (9) from Boulliung and Wood (2023a), using data from Boulliung and Wood (2022)
T, X_{sil}	1200–1500	1	Anhydrous basalt to rhyolite	Eq. (11) from Boulliung and Wood (2023a), using data from Boulliung and Wood (2022)

Table S11. Solubility constants for H_2, CO, CH_4, H_2S, and noble gases and range of conditions of experiments used for calibration.

Variables	T (°C)	P (bars)	Composition	Reference

H_2				
P	1400–1450	7000–30000	Basalt (Fe-free)	Table S4 from Hughes et al. (2024b) based on data from Hirschmann et al. (2012)
P	1400	10000–30000	Andesite (Fe-free)	
CO				
P	1340–1617	350–32000	Basalt	Table S4 from Hughes et al. (2024b) based on data from Armstrong et al. (2015), Stanley et al. (2014), and Wetzel et al. (2013)
CH_4				
P	1400–1450	7000–30000	Basalt (Fe-free)	Eq. (7a) from Ardia et al. (2013)
C_{H2S}				
Constant	1050	2980–3120	Basalt	Fig. S6 from Hughes et al. (2024b) based on data from Lesne et al. (2015) and Moune et al. (2009)
Constant	1050	2040–3040	Basaltic andesite	
"X"				
Constant	1200	49–308	Ar in basalt	Figure S11, based on data from Iacono-Marziano et al. (2010)
Constant	1200	104–360	Ar in rhyolite	Figure S11, based on data from Iacono-Marziano et al. (2010)
Constant	1200	68–296	Ne in basalt	Figure S11, based on data from Iacono-Marziano et al. (2010)
Constant	1200	100–299	Ne in rhyolite	Figure S11, based on data from Iacono-Marziano et al. (2010)

Table S12. Oxygen fugacity (f_{O2}) to Fe^{3+}/Fe^{2+} relationships and their calibration ranges.

Variables	*T* (°C)	*P* (bars)	Composition	Reference
T, *P*, X_{sil}	1200–1630	1	Basalt to andesite	Eq. (7) in Kress and Carmichael (1991)
T, *P*, X_{sil}	1200–1630	1	Basalt to andesite	Eq. (A-5,6) in Kress and Carmichael (1991)
T, *P*, X_{sil}	–	1	<60 wt% SiO_2	Eq. (9a) in O'Neill et al. (2018)
T, *P*, X_{sil}	1195–1636	1	Basalt to dacite	Eq. (4) in Borisov et al. (2018)

Table S13. Sulfide, anhydrite, and graphite saturation conditions and their calibration ranges.

Variables	T (°C)	P (bars)	Composition	Reference
Sulfide content at sulfide saturation*				
T, *P*, X_{sil}, X_{sulf}	1150–1800	1–55000	Anhydrous basalt to rhyolite	Eq. (10.34, 10.43, 10.45, 10.46) in O'Neill (2021) (with or without dilution from H_2O) (option to use PySulfSat; Wieser and Gleeson, 2023)
T, *P*, X_{sil}, H_2O X_{sulf}	1045–1800	1–55000	Hydrous basalt to rhyolite	Eq. (10.34, 10.43, 10.45, 10.46, 10.49) in O'Neill (2021)

T, P, X_{sil}, H_2O	785–1500	1–20000	Hydrous basalt to rhyolite	Eq. (9) in Liu et al. (2007)
T, P, X_{sil}, H_2O	1050–1800	1–90000	Hydrous Basalt to rhyolite	Eq. (7) Fortin et al. (2015) (option to use PySulfSat; Wieser and Gleeson, 2023)
T, P, H_2O, X_{sulf}	1250–1400	10000–25000	Hydrous basalt	Eq. (2) Liu et al. (2021) (option to use PySulfSat; Wieser and Gleeson, 2023)
T, P, X_{sil}, X_{sulf}	1150–1800	1–55000	Anhydrous basalt to rhyolite	O'Neill and Mavrogenes (2022) using PySulfSat; Wieser and Gleeson, 2023)
T, X_{sil}	1150–2160	1–240000	Hydrous basalt to rhyolite	Smythe et al. (2017) using PySulfSat by Wieser and Gleeson, 2023)
Sulfate content at anhydrite saturation				
T, X_{sil}, H_2O	700–1325	1000–30000	Basalt to rhyolite	Eq. (8) using Table 5 in Chowdhury and Dasgupta (2019) option to use PySulfSat; Wieser and Gleeson, 2023)
T, X_{sil}, H_2O	700–1325	300–30000	Basalt to rhyolite	Eq. (8–14) in Zajacz and Tsay (2019) (option to use PySulfSat; Wieser and Gleeson, 2023)
T, X_{sil}, H_2O	700–1350	300–50000	Basalt to rhyolite	Eq. (4) in Liu et al. (2023)
Graphite saturation				
P, T	–	–	n/a	Eq. (3) K_I in Holloway et al. (1992)

Note: *If sulfide composition is required, it is assumed to be pure FeS unless specificed by the user.

2 Degassing and regassing calculations

We start each re- or degassing calculation by determining P^v_{sat} and the speciation of the volatiles in the melt at P^v_{sat} as described in Hughes et al. (2024). This sets the bulk composition of the system, especially for oxygen, which is distributed between the volatiles (i.e., $CO_{2,T}$, H_2O_T, SO_4^{2-}, and CO) and iron (i.e., FeO and $FeO_{1.5}$) in the melt:

$$w^m_{O_T} = M_O \left(\frac{2w^m_{CO_{2,T}}}{M_{CO_2}} + \frac{w^m_{CO}}{M_{CO}} + \frac{w^m_{H_2O_T}}{M_{H_2O}} + \frac{3w^m_{SO_3}}{M_{SO_3}} + \frac{w^T_{Fe}}{M_{Fe}} \left(\frac{1.5\left(\frac{Fe^{3+}}{Fe^{2+}}\right) + 1}{\left(\frac{Fe^{3+}}{Fe^{2+}}\right) + 1} \right) \right) \quad \text{(S1)}$$

where w^m_i is the weight fraction of species i (indicated by the subscript) in the melt (m – indicated by the superscript) and M_i is the molecular mass of species i. Note that this mass balance constraint does not include oxygen in the silicate melt component which does not exchange between melt and vapor, as this does not partake in degassing. For molecular species (e.g., CO, FeO, and $FeO_{1.5}$), all oxygen present in the species is counted towards the oxygen budget. For the ionic species (CO_3^{2-} and SO_4^{2-}), all but one of the oxygens is counted towards the oxygen budget – the final oxygen is associated with silicate component (e.g., CaO, Na_2O), which does not exchange between the melt and vapor and hence is not included in the oxygen budget (i.e., they are treated as CO_2 and SO_3). All oxygen present in H_2O_T is included in the oxygen budget. For H_2O_{mol}, this is as the case of the other molecular species.

For OH^-, the additional oxygen comes from the silicate component, as for the other ionic species, and therefore does not need to be counted in the oxygen budget.

If the inputted melt composition (including volatiles and f_{O2} estimate) does not represent the bulk composition (i.e., there is vapor present), the vapor must be added back to calculate the bulk composition. Mass balance for each component distributed between melt and vapor is given by:

$$w_i^T = M_i \left(w_v^{\mathrm{T}} \left(\left(\frac{X_i^v}{X_T^v} \right) - X_i^m \right) + X_i^m \right), \tag{S2}$$

where i refers to the i^{th} component (i.e., C, H, S, O, or "X"); w_i^T is the total weight fraction of this component; M_i is the molar mass of i; w_v^{T} is the weight fraction of vapor in the system; X_i^v is the mole of i in the vapor (uppercase, italic X denotes mole, whereas "X" denotes the species "X"); X_T^v is the moles of vapor; and X_i^m is the moles of i in the melt (e.g., Burgisser et al., 2015; Liggins et al., 2020).

For carbon, i = C and in the vapor:

$$X_{\mathrm{C}}^v = x_{\mathrm{CO_2}}^v + x_{\mathrm{CO}}^v + x_{\mathrm{CH_4}}^v + x_{\mathrm{OCS}}^v, \tag{S3}$$

where x_{j}^v is the mole fraction of species j in the vapor, and in the melt:

$$X_{\mathrm{C}}^m = \frac{w_{\mathrm{CO_{2,T}}}^m}{M_{\mathrm{CO_{2,T}}}} + \frac{w_{\mathrm{CH_4}}^m}{M_{\mathrm{CH_4}}} + \frac{w_{\mathrm{CO}}^m}{M_{\mathrm{CO}}}. \tag{S4}$$

For hydrogen, i = H and

$$X_{\mathrm{H}}^v = x_{\mathrm{H_2O}}^v + x_{\mathrm{H_2}}^v + 2x_{\mathrm{CH_4}}^v + x_{\mathrm{H_2S}}^v, \tag{S5}$$

$$X_{\mathrm{H}}^m = \frac{w_{\mathrm{H_2O_T}}^m}{M_{\mathrm{H_2O}}} + \frac{w_{\mathrm{H_2}}^m}{M_{\mathrm{H_2}}} + \frac{2w_{\mathrm{CH_4}}^m}{M_{\mathrm{CH_4}}} + \frac{w_{\mathrm{H_2S}}^m}{M_{\mathrm{H_2S}}}. \tag{S6}$$

For sulfur, i = S and

$$X_{\mathrm{S}}^v = x_{\mathrm{SO_2}}^v + 2x_{\mathrm{S_2}}^v + x_{\mathrm{H_2S}}^v + x_{\mathrm{OCS}}^v, \tag{S7}$$

$$X_{\mathrm{S}}^m = \frac{w_{\mathrm{SO_4^{2-}}}^m}{M_{\mathrm{SO_4^{2-}}}} + \frac{w_{*\mathrm{S^{2-}}}^m}{M_{*\mathrm{S^{2-}}}} + \frac{w_{\mathrm{H_2S}}^m}{M_{\mathrm{H_2S}}}. \tag{S8}$$

For oxygen i = O, such that

$$X_{\mathrm{O}}^v = 2x_{\mathrm{O_2}}^v + 2x_{\mathrm{CO_2}}^v + x_{\mathrm{CO}}^v + x_{\mathrm{OCS}}^v + x_{\mathrm{H_2O}}^v + 2x_{\mathrm{SO_2}}^v, \tag{S9}$$

$$X_{\mathrm{O}}^{m} = \frac{2w_{\mathrm{CO_{2,T}}}^{m}}{M_{\mathrm{CO_{2,T}}}} + \frac{w_{\mathrm{CO}}^{m}}{M_{\mathrm{CO}}} + \frac{w_{\mathrm{H_2O_T}}^{m}}{M_{\mathrm{H_2O}}} + \frac{3w_{\mathrm{SO_4^{2-}}}^{m}}{M_{\mathrm{SO_4^{2-}}}} + \frac{w_{\mathrm{Fe}}^{T}}{M_{\mathrm{Fe}}}\left(\frac{1.5\left(\frac{\mathrm{Fe^{3+}}}{\mathrm{Fe^{2+}}}\right)+1}{\left(\frac{\mathrm{Fe^{3+}}}{\mathrm{Fe^{2+}}}\right)+1}\right). \quad \text{(S10)}$$

1650 And for species "X", *i* = "X" and

$$X_{\text{"X"}}^{v} = x_{\text{"X"}}^{v}, \quad \text{(S11)}$$

$$X_{\text{"X"}}^{m} = \frac{w_{\text{"X"}}^{m}}{M_{\text{"X"}}}. \quad \text{(S12)}$$

1651

1652 At each *P*, the mass balance constraint for each component distributed between melt and vapor
1653 must be satisfied as described in eq. (S2–12).

1654

1655 Here we outline the approach for calculating vapor and melt compositions and proportions
1656 described in Section 4.2 of the main text in more detail (a flow chart of this calculation is shown in
1657 Figure 4 of the main text).

1658 1) The inputs for the calculation are *T*, major element composition of the melt, concentrations of
1659 volatile components in the melt (H_2O-eq, CO_2-eq, and S-eq), f_{O2} or Fe^{3+}/Fe_T. The step-size of *P* can
1660 also be set (default = 10 bars). Options are either closed- or open-system re- or degassing.
1661 2) P^vsat and the melt/vapor speciation is calculated.
1662 3) Bulk composition of the system is calculated, either:
1663 a) The melt composition at P^v_{sat} is the bulk composition of the system, or
1664 b) The proportion of vapor present at P^v_{sat} is given, which is inputted as w^T_g in eq. (S2) as well as
1665 the melt and vapor composition calculated at P^v_{sat}, enabling w^T_i's for all volatiles (i.e., C, O, S,
1666 and H) to be calculated, or
1667 c) The initial amount of CO_2-eq in the melt is given, in which case eq. (S2) is used to calculate
1668 w^T_g given w^T_C and the melt and vapor composition at P^v_{sat}. Then the w^T_i's for all volatiles (i.e.,
1669 O, S, and H) to be calculated using eq. (S2).
1670 4) *P* is de/increased.
1671 5) x^v_i's are calculated:
1672 a) Initial guesses for x^v_{O2}, x^v_{CO}, and x^v_{S2} are taken from the previous *P* step.
1673 b) Equilibrium constants (K_i) and fugacity coefficients (y_i) are calculated at the given *T* and *P*.
1674 c) Using y_i and *P*, x^v_{O2}, x^v_{CO}, and x^v_{S2} in eq. (1, 4, 5) are used to calculate x^v_{CO2} and x^v_{SO2}, from
1675 which x^v_{OCS} can be calculated using eq. (1, 8).
1676 d) Given the sum of all x^v_i's must be one, x^v_{H2O} can be calculated using eq. (1, 3–8), from which
1677 x^v_{H2}, x^v_{H2S}, and x^v_{CH4} can be calculated using the same equations.
1678 e) Using y_i and *P* in eq. (1), x^v_{O2}, x^v_{CO}, and x^v_{S2} are converted to f_{O2}, f_{CO}, and f_{S2}.
1679 6) w^m_i's are calculated:
1680 a) Solubility (C_i) and equilibrium, (K_i) constants are calculated at the given *T*, *P*, and melt
1681 composition.
1682 b) All x^v_i's are converted to f_i's using eq. (1).
1683 c) Each w^m_i's is calculated from the appropriate equation in eq. (9–10, 12–13, 15–18).
1684 d) Fe^{3+}/Fe_T is calculated.
1685 7) Iteration to find solution:

a) Weight fraction of gas (w^T_g) implied for each volatile (i.e., C, H, O, and S) is calculated from eq. (17) using x^v_i's and w^m_i.
b) Difference between w^T_g based on C and each other volatile (i.e., H, O, and S) is calculated. If the difference is below the specified tolerance, the solution has been found.
c) If the solution has not been found, new guesses for x^v_{O2}, x^v_{CO}, and x^v_{S2} are created using a Newton Raphson/Jacobian Matrix approach, and steps 5–7 are repeated.
d) If a solution cannot be found after 100 iterations, the Newton Raphson step size is reduced by a factor of ten. If a solution still cannot be found, the guessed species are switched to x^v_{O2}, x^v_{H2}, and x^v_{S2} or x^v_{O2}, x^v_{CO}, and x^v_{H2}. If a solution still cannot be found, the calculation is terminated.

8) Once solution has been found, melt and vapor composition and proportions are calculated. Return to step 4 until final P is reached.

3 Example reference table for calculations

Table S14. Parameterisations used for model dependent variables in calculations using VolFe.

Model dependent variable	Reference
O_2 fugacity coefficient	Shi and Saxena (1992)
CO fugacity coefficient	Shi and Saxena (1992)
H_2 fugacity coefficient	Shaw and Wones (1964)
S_2 fugacity coefficient	Shi and Saxena (1992)
CO_2 fugacity coefficient	Shi and Saxena (1992)
H_2O fugacity coefficient	Holland and Powell (1991)
SO_2 fugacity coefficient	Shi and Saxena (1992) as modified in Hughes et al. (2022)
CH_4 fugacity coefficient	Shi and Saxena (1992)
H_2S fugacity coefficient	Shi and Saxena (1992) as modified in Hughes et al. (2024)
OCS fugacity coefficient	Shi and Saxena (1992)
CO_2 equilibrium constant	Reaction (c) in Table 1 of Ohmoto and Kerrick (1977)
H_2O equilibrium constant	Reaction (d) in Table 1 of Ohmoto and Kerrick (1977)
SO_2 equilibrium constant	Reaction (f) in Table 1 of Ohmoto and Kerrick (1977)
CH_4 equilibrium constant	Reaction (e) in Table 1 of Ohmoto and Kerrick (1977)
H_2S equilibrium constant	Reaction (h) in Table 1 of Ohmoto and Kerrick (1977)
OCS equilibrium constant	Eq. (8) in Moussallam et al. (2019)
H_2O_T solubility constant	Hughes et al. (2024)
$CO_{2,T}$ solubility constant	Dixon et al. (1995)
$H_{2,mol}$ solubility constant	Hughes et al. (2024)
CO_{mol} solubility constant	Hughes et al. (2024)
$CH_{4,mol}$ solubility constant	Eq. (7a) from Ardia et al. (2013)
$*S^{2-}$ solubility constant	Eq. (10.43) from O'Neill (2021) (including the effect of H_2O dilution)
SO_4^{2-} solubility constant	Eq. (12a) from O'Neill and Mavrogenes (2022) (including the effect of H_2O dilution)
H_2S_{mol} solubility constant	Hughes et al. (2024)
$CO_{2,T}$ speciation constant	All CO_3^{2-} as basalt
Fe^{3+}/Fe_T	Eq. A-5 and A-6 from Kress and Carmichael (1991)
FMQ buffer	Frost (1991)
S^{2-}CSS	Eq. (10.34, 10.43, 10.45, 10.46) in O'Neill (2021)
S^{6+}CAS	Eq. (8) in Chowdhury and Dasgupta (2019)

Graphite equilibrium constant	Eq. (3) from Holloway et al. (1992)

Notes: Melt species considered were H_2O_T, OH^-, $CO_{2,mol}$, CO_3^{2-}, $H_{2,mol}$, CO_{mol}, $CH_{4,mol}$, $*S^{2-}$, SO_4^{2-}, and H_2S_{mol}; vapor species considered were O_2, CO, H_2, S_2, CO_2, H_2O, SO_2, CH_4, H_2S, and OCS.

4 References

Allison, C.M., Roggensack, K., Clarke, A.B., 2022. MafiCH: a general model for H2O–CO2 solubility in mafic magmas. Contrib. to Mineral. Petrol. 177, 1–22. https://doi.org/10.1007/S00410-022-01903-Y/FIGURES/10

Allison, C.M., Roggensack, K., Clarke, A.B., 2019. H2O–CO2 solubility in alkali-rich mafic magmas: new experiments at mid-crustal pressures. Contrib. to Mineral. Petrol. 174, 58. https://doi.org/10.1007/s00410-019-1592-4

Armstrong, L.S., Hirschmann, M.M., Stanley, B.D., Falksen, E.G., Jacobsen, S.D., 2015. Speciation and solubility of reduced C-O-H-N volatiles in mafic melt: Implications for volcanism, atmospheric evolution, and deep volatile cycles in the terrestrial planets. Geochim. Cosmochim. Acta 171, 283–302. https://doi.org/10.1016/j.gca.2015.07.007

Behrens, H., Ohlhorst, S., Holtz, F., Champenois, M., 2004. CO2 solubility in dacitic melts equilibrated with H2O-CO2 fluids: Implications for modeling the solubility of CO2 in silicic melts. Geochim. Cosmochim. Acta 68, 4687–4703. https://doi.org/10.1016/J.GCA.2004.04.019

Blank, J.G., 1993. An experimental investigation of the behaviour of carbon dioxide in rhyolitic melt. California Institute of Technology.

Blank, J.G., Delaney, J.R., Marais, D.J.D., 1993a. The concentration and isotopic composition of carbon in basaltic glasses from the Juan de Fuca Ridge, Pacific Ocean. Geochim. Cosmochim. Acta 57, 875–887. https://doi.org/10.1016/0016-7037(93)90175-V

Blank, J.G., Stolper, E.M., Carroll, M.R., 1993b. Solubilities of carbon dioxide and water in rhyolitic melt at 850°C and 750 bars. Earth Planet. Sci. Lett. 119, 27–36. https://doi.org/10.1016/0012-821X(93)90004-S

Borisov, A., Behrens, H., Holtz, F., 2018. Ferric/ferrous ratio in silicate melts: a new model for 1 atm data with special emphasis on the effects of melt composition. Contrib. to Mineral. Petrol. 173, 1–15. https://doi.org/10.1007/S00410-018-1524-8/FIGURES/10

Botcharnikov, R.E., Behrens, H., Holtz, F., 2006. Solubility and speciation of C–O–H fluids in andesitic melt at T = 1100–1300 °C and P = 200 and 500 MPa. Chem. Geol. 229, 125–143. https://doi.org/10.1016/J.CHEMGEO.2006.01.016

Boulliung, J., Wood, B.J., 2023a. Sulfur oxidation state and solubility in silicate melts. Contrib. to Mineral. Petrol. 178, 1–15. https://doi.org/10.1007/S00410-023-02033-9/FIGURES/9

Boulliung, J., Wood, B.J., 2023b. Corrigendum to "SO2 solubility and degassing behavior in silicate melts" [Geochim. Cosmochim. Acta 336 (2022) 150–164]. Geochim. Cosmochim. Acta 343,

420. https://doi.org/10.1016/J.GCA.2022.11.025
Boulliung, J., Wood, B.J., 2022. SO2 solubility and degassing behavior in silicate melts. Geochim. Cosmochim. Acta Vol. , 1 Novemb. 2022, Pages 150-164 336, 150–164. https://doi.org/10.1016/j.gca.2022.08.032
Burgisser, A., Alletti, M., Scaillet, B., 2015. Simulating the behavior of volatiles belonging to the C–O–H–S system in silicate melts under magmatic conditions with the software D-Compress. Comput. Geosci. 79, 1–14. https://doi.org/10.1016/J.CAGEO.2015.03.002
Chowdhury, P., Dasgupta, R., 2019. Effect of sulfate on the basaltic liquidus and Sulfur Concentration at Anhydrite Saturation (SCAS) of hydrous basalts – Implications for sulfur cycle in subduction zones. Chem. Geol. 522, 162–174. https://doi.org/10.1016/J.CHEMGEO.2019.05.020
Dixon, J.E., 1997. Degassing of alkalic basalts. Am. Mineral. 82, 368–378. https://doi.org/10.2138/AM-1997-3-415/MACHINEREADABLECITATION/RIS
Dixon, J.E., Stolper, E.M., Holloway, J.R., 1995. An experimental study of water and carbon dioxide solubilities in mid-ocean ridge basaltic liquids. Part I: Calibration and solubility models. J. Petrol. 36, 1607–1631. https://doi.org/10.1093/oxfordjournals.petrology.a037267
Fine, G., Stolper, E., 1986. Dissolved carbon dioxide in basaltic glasses: concentrations and speciation. Earth Planet. Sci. Lett. 76, 263–278. https://doi.org/10.1016/0012-821X(86)90078-6
Fogel, R.A., Rutherford, M.J., 1990. The solubility of carbon dioxide in rhyolitic melts; a quantitative FTIR study. Am. Mineral. 75, 1311–1326.
Fortin, M.A., Riddle, J., Desjardins-Langlais, Y., Baker, D.R., 2015. The effect of water on the sulfur concentration at sulfide saturation (SCSS) in natural melts. Geochim. Cosmochim. Acta 160, 100–116. https://doi.org/10.1016/J.GCA.2015.03.022
Haughton, D.R., Roeder, P.L., Skinner, B.J., 1974. Solubility of Sulfur in Mafic Magmas. Econ. Geol. 69, 451–467. https://doi.org/10.2113/GSECONGEO.69.4.451
Hirschmann, M.M., Withers, A.C., Ardia, P., Foley, N.T., 2012. Solubility of molecular hydrogen in silicate melts and consequences for volatile evolution of terrestrial planets. Earth Planet. Sci. Lett. 345–348, 38–48. https://doi.org/10.1016/J.EPSL.2012.06.031
Holland, T., Powell, R., 1991. A Compensated-Redlich-Kwong (CORK) equation for volumes and fugacities of CO2 and H2O in the range 1 bar to 50 kbar and 100–1600°C. Contrib. to Mineral. Petrol. 1991 1092 109, 265–273. https://doi.org/10.1007/BF00306484
Holloway, J.R., Blank, J.G., 1994. Application of experimental results to C-O-H species in natural melts. Rev. Mineral. Geochemistry1 30, 187–230.
Holloway, J.R., Pan, V., Gudmundsson, G.B., 1992. High-pressure fluid-absent melting experiments in the presence of graphite: oxygen fugacity, ferric/ferrous ratio and dissolved CO2. Eur. J. Mineral. 4, 105–114.
Hughes, E.C., Liggins, P., Saper, L., Stolper, E.M., 2024. The effects of oxygen fugacity and sulfur on the pressure of vapor-saturation of magma. Am. Mineral. 109, 422–438.

Hughes, E.C., Saper, L.M., Liggins, P., O'Neill, H.S.C., Stolper, E.M., 2022. The sulfur solubility minimum and maximum in silicate melt. J. Geol. Soc. London. 180, jgs2021-125. https://doi.org/https://doi.org/10.1144/jgs2021-125

Iacono-Marziano, G., Paonita, A., Rizzo, A., Scaillet, B., Gaillard, F., 2010. Noble gas solubilities in silicate melts: New experimental results and a comprehensive model of the effects of liquid composition, temperature and pressure. Chem. Geol. 279, 145–157. https://doi.org/10.1016/J.CHEMGEO.2010.10.017

Kadik, A.A., Lukanin, O.A., Lebedev, Y.B., Korovushkina, E.Y., 1972. Solubility of H2O and CO2 in granite and basalt melts at high pressures. Geochem. Int. 9, 1041–1050.

Kress, V.C., Carmichael, I.S.E., 1991. The compressibility of silicate liquids containing Fe2O3 and the effect of composition, temperature, oxygen fugacity and pressure on their redox states. Contrib. to Mineral. Petrol. 108, 82–92. https://doi.org/10.1007/BF00307328

Lesne, P., Scaillet, B., Pichavant, M., 2015. The solubility of sulfur in hydrous basaltic melts. Chem. Geol. 418, 104–116. https://doi.org/10.1016/J.CHEMGEO.2015.03.025

Lesne, P., Scaillet, B., Pichavant, M., Brey, G.P., 2011. The carbon dioxide solubility in alkali basalts: an experimental study. Contrib. to Mineral. Petrol. 162, 153–168. https://doi.org/10.1007/s00410-010-0585-0

Liggins, P., Shorttle, O., Rimmer, P.B., 2020. Can volcanism build hydrogen-rich early atmospheres? Earth Planet. Sci. Lett. 550, 116546. https://doi.org/10.1016/J.EPSL.2020.116546

Liu, K., Zhang, L., Guo, X., Ni, H., 2021. Effects of sulfide composition and melt H2O on sulfur content at sulfide saturation in basaltic melts. Chem. Geol. 559, 119913. https://doi.org/10.1016/j.chemgeo.2020.119913

Liu, K., Zhang, L., Ni, H., 2023. Anhydrite solubility enhanced by CaO in silicate melts: Implications for sulfur cycling in subduction zones. Geochim. Cosmochim. Acta 349, 135–145. https://doi.org/10.1016/J.GCA.2023.04.007

Liu, Y., Samaha, N.T., Baker, D.R., 2007. Sulfur concentration at sulfide saturation (SCSS) in magmatic silicate melts. Geochim. Cosmochim. Acta 71, 1783–1799. https://doi.org/10.1016/J.GCA.2007.01.004

Moune, S., Holtz, F., Botcharnikov, R.E., 2009. Sulphur solubility in andesitic to basaltic melts: implications for Hekla volcano. Contrib. to Mineral. Petrol. 157, 691–707. https://doi.org/10.1007/s00410-008-0359-0

Moussallam, Y., Oppenheimer, C., Scaillet, B., 2019. On the relationship between oxidation state and temperature of volcanic gas emissions. Earth Planet. Sci. Lett. 520, 260–267. https://doi.org/10.1016/J.EPSL.2019.05.036

O'Neill, H.S.C., 2021. The thermodynamic controls on sulfide saturation in silicate melts with application to Ocean Floor Basalts., in: Moretti, R., Neuville, D.R. (Eds.), Magma Redox Geochemistry, Geophysical Monograph Series. John Wiley & Sons, Inc., pp. 177–213.

https://doi.org/10.1002/9781119473206.ch10
O'Neill, H.S.C., Berry, A.J., Mallmann, G., 2018. The oxidation state of iron in Mid-Ocean Ridge Basaltic (MORB) glasses: Implications for their petrogenesis and oxygen fugacities. Earth Planet. Sci. Lett. 504, 152–162. https://doi.org/10.1016/J.EPSL.2018.10.002
O'Neill, H.S.C., Mavrogenes, J.A., 2022. The sulfate capacities of silicate melts. Geochim. Cosmochim. Acta. https://doi.org/10.1016/J.GCA.2022.06.020
O'Neill, H.S.C., Mavrogenes, J.A., 2002. The sulfide capacity and the sulfur content at sulfide saturation of silicate melts at 1400°C and 1 bar. J. Petrol. 43, 1049–1087. https://doi.org/10.1093/petrology/43.6.1049
Ohmoto, H., Kerrick, D.M., 1977. Devolatilization equilibria in graphitic systems. Am. J. Sci. 277, 1013–1044. https://doi.org/10.2475/AJS.277.8.1013
Pan, V., Holloway, J.R., Hervig, R.L., 1991. The pressure and temperature dependence of carbon dioxide solubility in tholeiitic basalt melts. Geochim. Cosmochim. Acta 55, 1587–1595. https://doi.org/10.1016/0016-7037(91)90130-W
Shaw, H.R., Wones, D.R., 1964. Fugacity coefficients for hydrogen gas between 0 degrees and 1000 degrees C, for pressures to 3000 atm. Am. J. Sci. 262, 918–929. https://doi.org/10.2475/AJS.262.7.918
Shi, P., Saxena, S.K., 1992. Thermodynamic modeing of the C-H-O-S fluid system. Am. Mineral. 77, 1038–1049.
Shishkina, T.A., Botcharnikov, R.E., Holtz, F., Almeev, R.R., Portnyagin, M.V., 2010. Solubility of H2O- and CO2-bearing fluids in tholeiitic basalts at pressures up to 500 MPa. Chem. Geol. 277, 115–125. https://doi.org/10.1016/J.CHEMGEO.2010.07.014
Silver, L.A., Ihinger, P.D., Stolper, E.M., 1990. The influence of bulk composition on the speciation of water in silicate glasses. Contrib. to Mineral. Petrol. 104, 142–162. https://doi.org/10.1007/BF00306439
Smythe, D.J., Wood, B.J., Kiseeva, E.S., 2017. The S content of silicate melts at sulfide saturation: New experiments and a model incorporating the effects of sulfide composition. Am. Mineral. 102, 795–803. https://doi.org/10.2138/AM-2017-5800CCBY
Stanley, B.D., Hirschmann, M.M., Withers, A.C., 2014. Solubility of COH volatiles in graphite-saturated martian basalts. Geochim. Cosmochim. Acta 129, 54–76. https://doi.org/10.1016/j.gca.2013.12.013
Thibault, Y., Holloway, J.R., 1994. Solubility of CO2 in a Ca-rich leucitite: effects of pressure, temperature, and oxygen fugacity. Contrib. to Mineral. Petrol. 116, 216–224. https://doi.org/10.1007/BF00310701/METRICS
Tuff, J., O'Neill, H.S.C., 2010. The effect of sulfur on the partitioning of Ni and other first-row transition elements between olivine and silicate melt. Geochim. Cosmochim. Acta 74, 6180–6205. https://doi.org/10.1016/J.GCA.2010.08.014

Wetzel, D.T., Rutherford, M.J., Jacobsen, S.D., Hauri, E.H., Saal, A.E., 2013. Degassing of reduced carbon from planetary basalts. Proc. Natl. Acad. Sci. 110, 8010–8013. https://doi.org/10.1073/PNAS.1219266110

Wieser, P.E., Gleeson, M., 2023. PySulfSat: An open-source Python3 tool for modeling sulfide and sulfate saturation. Volcanica 6, 107–127. https://doi.org/10.30909/VOL.06.01.107127

Witham, F., Blundy, J.D., Kohn, S.C., Lesne, P., Dixon, J.E., Churakov, S. V., Botcharnikov, R.E., 2012. SolEx: A model for mixed COHSCl-volatile solubilities and exsolved gas compositions in basalt. Comput. Geosci. 45, 87–97. https://doi.org/10.1016/j.cageo.2011.09.021

Zajacz, Z., Tsay, A., 2019. An accurate model to predict sulfur concentration at anhydrite saturation in silicate melts. Geochim. Cosmochim. Acta 261, 288–304. https://doi.org/10.1016/J.GCA.2019.07.007